UNIVERSITA' DEGLI STUDI DI NAPOLI "FEDERICO II"

DEPARTMENT OF CHEMICAL, MATERIALS AND PRODUCTION ENGINEERING (DICMAPI)

PHD IN "INDUSTRIAL PRODUCT AND PROCESS ENGINEERING"
XXXVI CYCLE

"CONTROLLED CELL MECHANO-MODULATOR FOR MECHANOMEDICINE APPLICATIONS"

Supervisor
Dr. Carlo F. Natale, PhD
Eng. Valeria Panzetta, PhD
Ch.mo Prof. Paolo Antonio Netti, PhD

Coordinator
Ch.mo Prof. Andrea D'Anna, PhD

Candidate
Luigi Crimaldi

November 2020 - January 2024

Table of contents

Chapter 1

Introduction

1.1 Mechanomedicine

Human body is constantly subjected to a wide range of mechanical forces, fundamental for its development and physiological function. Examples are abundant, such as compressive loads borne by cartilage and bones during everyday activities like walking and exercise. Similarly, dermal tissue experiences tensile, compressive, and shearing forces as we engage with the environment and breathing imposes cyclic stretching on lungs, underlining the ubiquity of mechanical interactions within the human body.

The remarkable capacity of tissues to adapt and remodel in response to changes in mechanical forces has profound implications for their patho-physiological behavior. Bone, for instance, alters its shape, density, and stiffness in response to variation of mechanical loading[1,2] and blood vessels reconfigure themselves in response to changes in blood pressure and shear stress[3,4]. These adaptations deeply impact tissue's structure and function and they are essential for maintaining tissue homeostasis. On the other hand, deviations from physiological mechanical loading conditions can lead to a spectrum of tissue and organ pathologies, such as osteoporosis, osteoarthritis, tendinopathy, atherosclerosis, and fibrosis[5].

Mechanomedicine, an emerging field at the intersection of biomechanics and medical science, seeks to unravel the intricate relationship existing between mechanical forces and biological functions, with the final goal to utilize the acquired information to enhance health. This interdisciplinary field has gained increasing attention due to its potential to unveil novel therapeutic strategies grounded on the administration of mechanical cures, known as mechanotherapy.

Mechanomedicine finds a first practical application in orthopedics, particularly in the rehabilitation of musculoskeletal injuries. Therapeutic exercises and interventions are designed to capitalize on mechanical principles, promoting tissue healing and its functional recovery. Moreover, controlled mechanical loading in postoperative rehabilitation enhances the adaptive response of tendons and ligaments, contributing to restore their functionalities, improve physical activity, reduce pain, and increase patient satisfaction[6–9]. On the same line, the application of mechanomedicine's principles in

the tissue engineering field reveals innovative possibilities. In fact, several studies[10,11] highlighted the importance to integrate biomechanical cues, such as mechanical ones, into scaffold design to guide and to improve tissue regeneration. Biophysical stimuli, mimicking the native mechanical microenvironment, are harnessed to optimize the correct development of functional tissues, offering promising avenues for regenerative medicine.

At this point, it becomes relevant to understand how mechanical signals act and how such stimulation should be delivered in order to guide tissue response. To do this, we should understand what happens at cellular level, recognizing cells as the fundamental building blocks of tissues and organs. Indeed, cells act as intermediaries in the translation of mechanical stimuli into biochemical signals. They are able to sense and interpret the mechanical cues of the extracellular matrix (ECM) and, in turn, actively engage with the ECM, initiating a cascade of events that define tissue's architectural and functional landscape. Therefore, unrevealing the mechanisms behind cell response to mechanical signals and the dynamic crosstalk with the ECM becomes pivotal for fostering a deeper understanding of disease processes, and ultimately developing effective interventions in the realm of mechanomedicine.

1.2 Cell mechanobiology

Cells, as the fundamental constituents of organized tissues and organs, are not passive entities primarily engaged in consuming and proliferation, but they dynamically perceive and respond to external signals through the specific activation of specific biological processes. Besides chemical and biological signals, physical cues of ECM have a deep influence on cell behavior, directly regulating their functions and fate[12,13]. Over the last decades, the investigation of the complex interplay between mechanical forces and cell response has been the primary study object of the cell mechanobiology field.

A central element in mechanobiology is cellular mechanosensing, which describes the cell's ability in perceiving and transferring the mechanical cues arising from the ECM to the internal cellular components. The primary site of force transmission to the cell is the cellular membrane, where the direct contact with the ECM occurs. Force sensing produces the recruitment and clustering of specific cell transmembrane molecules, called integrins, that act as mechanoreceptors. Integrins' extracellular domains contact the ECM, while the cytoplasmic tails interact with discrete multiprotein complexes named focal adhesions (FAs), the main hub of mechanosensing activity. FAs (**Fig. 1.1 A**) are intricate intracellular structures comprising various scaffolding, docking, and signaling proteins, that are

collectively responsible for transferring mechanical stimuli from the surrounding extracellular environment to the cellular cytoskeleton. In particular, paxillin and focal adhesion kinase (FAK) proteins localize with the integrin cytoplasmic tails to recruit further signaling molecules and regulate actin cytoskeleton remodeling[14]. Other proteins, such as talin and vinculin, have a mechanosensitive function. Talin directly connects integrins to actin, it regulates adhesion strength and recruits vinculin under force[15]. This recruitment reinforces FAs, as vinculin crosslinks the talin molecule to the cytoskeleton actin filament[16].

Cell cytoskeleton (**Fig. 1.1 B**) is a dynamic structure composed by filamentous and crosslinking proteins. It provides mechanical support to the cells and controls their motility, shape, and tension balance[17]. The mechanical characteristic of the cytoskeleton strictly depends on the dynamics, configuration, and polarity of its constituents: actin fibers, microtubules, and intermediate filaments. Indeed, each of these elements exhibits a well-organized structure that contributes to the cell structural organization[18,19]. Cytoskeleton contractility, instead, is actuated by complex structures called stress fibers (SFs) and achieved through the interaction of actin fibers sliding along the motor protein myosin II[20,21]. The force generated in the actin cytoskeleton guides the clustering of integrins and, consequently, the maturation and stabilization of FAs[22].

The physical and biochemical linkage between integrins, FAs and cytoskeleton is essential to transmit ECM mechanical cues far beyond the plasma membrane to the cell nucleus which, by housing the cell's genome, can be referred as the cell's control center[23]. For this reason, the cell nucleus is emerging as the fundamental player for cellular mechanotransduction, i.e., the conversion of external physical stimuli into cell biochemical response. Mechanical inputs are transduced to the nucleus via several canonical ways, inducing the activation of transcription factors and their shuttling in and out the nucleus[24]. Moreover, the cytoskeleton network is directly attached to the nuclear membrane through the linker of nucleoskeleton and cytoskeleton (LINC) complex (**Fig. 1.1 C**), thereby allowing the direct transmission of mechanical forces[25,26]. The resulting nuclear deformations could alter chromatin structure and induce translocation of chromatin segments, thereby activating (or repressing) mechanosensitive genes[27].

Fluid shear stress, ECM stiffness and topography, tensile/compressive force are just a few of the mechanical cues involved in the cell–ECM crosstalk. These signals are perceived by cells and, through mechanotransduction processes, impact multiple biological responses including cell adhesion, migration, proliferation, differentiation, and ECM generation[28].

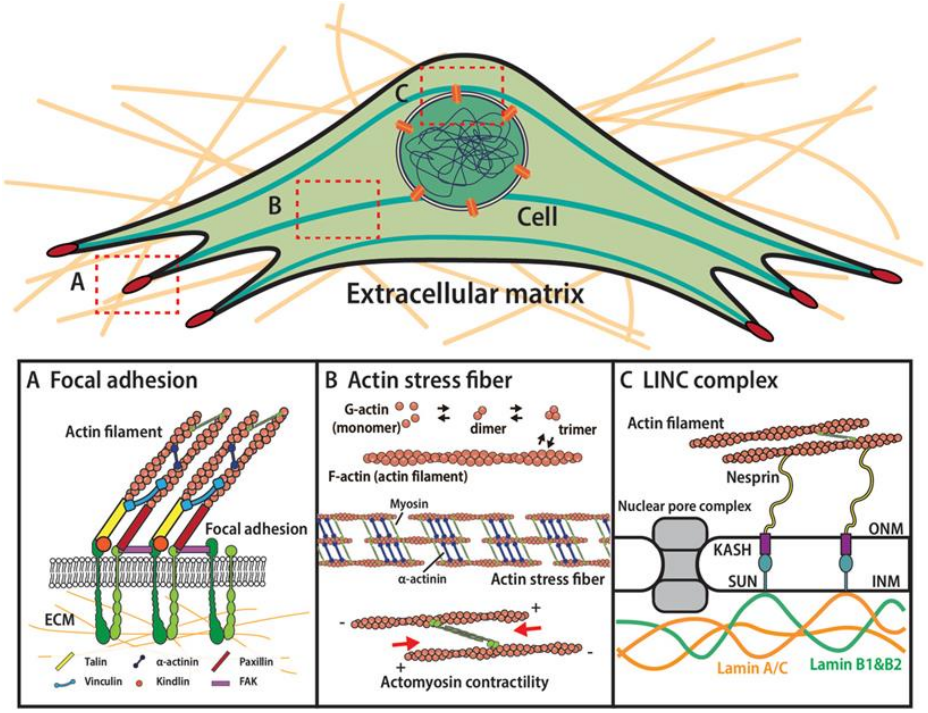

Fig. 1.1: *Intracellular molecular connection for cellular mechanosensing and mechanotransduction[32]. (A) Focal adhesion formation is induced by attachment between integrin and ECM. The formation and maturation of protein clusters, including vinculin, talin, FAK, paxillin, α-actinin, and kindlin are induced by integrin signaling that is regulated by mechanical signaling loop. (B) Molecular activity of myosin generates a contractile force in actin fibers, and highly regulated force generation by multiple myosins is used as the basis of cellular mechanical communication. C) Cytoskeleton is anchored to the nuclear membrane through the LINC molecular complex located in the nuclear membrane. The physical stimulus delivered by connected cytoskeleton is transmitted through the LINC complex into the nucleus, regulating various genetic activities.*

1.3 Challenges in the administration of a controlled mechanical dose to affect cell behavior

In pharmacology, cell-based drug screening is widely used for studying potential efficacy, safety, and mechanisms of action of pharmaceutical compounds[29]. Different chemical drug doses, defined as drug concentrations over cell density, are administered to cell cultures for a defined incubation time (typically 24–72 h). Cell response measurements involve careful quantification of biological endpoints which depend on the specific goals of the assay and the characteristics of the drug being tested. Common endpoints are, for example, cell viability or apoptosis, gene expression, protein production and enzyme activity[30,31]. These measurements serve as the foundation for constructing the dose-response curve, which graphically represents the drug dose and biological response relationship. Data are typically graphed with the dose or dose function (e.g., log10 dose) on the x-axis and the measured effect (response) on the y-axis. The curve's shape defines the drug's effectiveness and efficacy, giving important insights about the optimal drug dosage for therapeutic purposes.

Similarly, in the field of mechanobiology, efforts are concentrated in the calibration of mechanical stimulation to predict and affect cell functions and fate. The construction of a mechanical dose-response curve could allow researchers to precisely map the cellular responses across a spectrum of mechanical stimuli, enabling the development of targeted strategies to modulate cell behavior for desired outcomes and ultimately contributing to advancements in both basic science and clinical applications. However, the prescription of a mechanical dose to cells and the consequent realization of a dose-response curve appears to be more intricate.

Firstly, unlike the chemical pharmacological dose that is defined generally as a concentration, i.e. as a scalar quantity, mechanical dose is a second order tensor, defined by magnitude, direction and plane (normal or tangential). This imposes several challenges in achieving a uniform spatio-temporal presentation of a mechanical signal to the cell population. Indeed, ensuring that each cell experiences the same mechanical "dose", and timing of physical forces is essential to accomplish coherency in their biological response. On the cellular side, the intrinsic cell heterogeneity and anisotropy of the cell culture system further complicates this endeavor. In fact, conventional 2D cultures do not impose any specific spatial organization to cells, introducing variability in the cell population in terms of cell morphology and orientation. In this way, even if cells are uniformly stimulated, the different cellular mechanical state impacts on how cells perceive and respond to it. In the current literature, a large effort has been made during the last two decades to develop advanced technologies for in vitro manipulating cell mechanosensing and mechanotransduction mechanisms. In vitro cell mechanical stimulation tools serve as indispensable instruments for researchers aiming to mimic and manipulate the mechanical cues that cells experience in vivo. Unlike traditional static culture systems, these tools allow for the application of controlled and dynamic mechanical forces to cultured cells, enabling precise investigations of cellular responses triggered by mechanical stimuli. However, nowadays, an innovative tool able to administer controlled cellular mechanical doses and foster coherent cellular biological responses is still missing.

1.4 Project aims and outcomes

In contrast to traditional medicine, which relies primarily on the use of pharmaceuticals and chemical interventions to address diseases, mechanomedicine is a relatively newer paradigm that focuses on understanding and treating pathological processes through the administration of a new type of drug, namely mechanical stimulation. However, the applications of the mechanomedicine field are still

limited to specific research areas, as the fundamental mechanisms regulating the cellular biological response to mechanical signals are not fully understood.

As previously mentioned, cells possess the remarkable ability to integrate mechanical cues of the ECM which directly influence multiple cellular functions. For this reason, outlining the quantitative aspects of this relationship is crucial to how to actually modulate the mechanical stimuli to induce specific cellular responses. This knowledge not only advances our fundamental understanding of cell mechanobiology but also holds significant implications for various applications, including tissue engineering, regenerative medicine, and therapeutic interventions.

In this PhD thesis, we presented the realization of an advanced tool to characterize in vitro cellular response to mechanical stimulation. This device, identified as a cell stretching system, is able to administer mechanical doses to the cells ensuring a coherent cell perception of spatio-temporal controlled stretching stimuli. In this configuration, we also provided a meticulous approach to calibrate the cell mechanical stimulation which can be generalized for any cell type and mechanomedicine application.

Prior to delving into the core of the thesis, in the following chapter (**Chapter II**) it is provided an overview of the current state of art about the tools for in vitro cell mechanical stimulation. This section specifically concentrates on elucidating the working principles, design methodologies, biological relevance, as well as the inherent limitations of these devices.

Subsequently, in **Chapter III**, we offer a detailed description of the steps followed for the design and realization of the custom-made cell stretching system. Methodologies employed to overcome the challenges related to the microscope integration and live-cell imaging compatibility are provided. Moreover, this chapter illustrates the large efforts spent in creating a synergistic environment that enhances the consistency and reliability of cellular responses to mechanical stimulation.

By exploiting this powerful tool, in **Chapter IV**, we investigated the cell response to uniaxial sustained stretching. We focused our attention on quantitatively characterizing how the deformations applied to the substrate are dynamically perceived by the cells through the FAs and integrated at nuclear level by means of the actin cytoskeletal forces. Furthermore, morphological and biochemical changes of cell mechanosensory components were monitored over time to provide a better understanding of the mechanisms that regulate the cell mechanobiological response to mechanical stimulation.

In conclusion the directions for future perspective will be summarized.

1.5 References

1. Turner, C. H. & Pavalko, F. M. Mechanotransduction and functional response of the skeleton to physical stress: The mechanisms and mechanics of bone adaptation*. J. Orthop. Sci. 3, 346–355 (1998).

2. Mullender, M. et al. Mechanotransduction of bone cells in vitro: Mechanobiology of bone tissue. Med. Biol. Eng. Comput. 42, 14–21 (2004).

3. Owens, G. K. Role of Mechanical Strain in Regulation of Differentiation of Vascular Smooth Muscle Cells. Circ. Res. 79, 1054–1055 (1996).

4. Williams, B. Mechanical influences on vascular smooth muscle cell function: J. Hypertens. 16, 1921–1929 (1998).

5. Wang, J. H.-C. & Thampatty, B. P. An Introductory Review of Cell Mechanobiology. Biomech. Model. Mechanobiol. 5, 1–16 (2006).

6. Lamb, S. E. et al. Exercises to improve function of the rheumatoid hand (SARAH): a randomised controlled trial. The Lancet 385, 421–429 (2015).

7. The MOA Trial team et al. Exercise therapy, manual therapy, or both, for osteoarthritis of the hip or knee: a factorial randomised controlled trial protocol. Trials 10, 11 (2009).

8. Jansen, M. J., Viechtbauer, W., Lenssen, A. F., Hendriks, E. J. M. & De Bie, R. A. Strength training alone, exercise therapy alone, and exercise therapy with passive manual mobilisation each reduce pain and disability in people with knee osteoarthritis: a systematic review. J. Physiother. 57, 11–20 (2011).

9. French, H. P. et al. Exercise and Manual Physiotherapy Arthritis Research Trial (EMPART) for Osteoarthritis of the Hip: A Multicenter Randomized Controlled Trial. Arch. Phys. Med. Rehabil. 94, 302–314 (2013).

10. Butler, D. L. et al. The Impact of Biomechanics in Tissue Engineering and Regenerative Medicine. Tissue Eng. Part B Rev. 15, 477–484 (2009).

11. Liebschner, M., Bucklen, B. & Wettergreen, M. Mechanical Aspects of Tissue Engineering. Semin. Plast. Surg. 19, 217–228 (2005).

12. Hoffman, B. D. & Crocker, J. C. Cell Mechanics: Dissecting the Physical Responses of Cells to Force. Annu. Rev. Biomed. Eng. 11, 259–288 (2009).

13. Happe, C. L. & Engler, A. J. Mechanical Forces Reshape Differentiation Cues That Guide

Cardiomyogenesis. Circ. Res. 118, 296–310 (2016).

14. Kanchanawong, P. et al. Nanoscale architecture of integrin-based cell adhesions. Nature 468, 580–584 (2010).

15. Klapholz, B. & Brown, N. H. Talin – the master of integrin adhesions. J. Cell Sci. jcs.190991 (2017) doi:10.1242/jcs.190991.

16. Cohen, D. M., Kutscher, B., Chen, H., Murphy, D. B. & Craig, S. W. A Conformational Switch in Vinculin Drives Formation and Dynamics of a Talin-Vinculin Complex at Focal Adhesions. J. Biol. Chem. 281, 16006–16015 (2006).

17. Fletcher, D. A. & Mullins, R. D. Cell mechanics and the cytoskeleton. Nature 463, 485–492 (2010).

18. Fabry, B. et al. Scaling the Microrheology of Living Cells. Phys. Rev. Lett. 87, 148102 (2001).

19. Chen, T.-J., Wu, C.-C., Tang, M.-J., Huang, J.-S. & Su, F.-C. Complexity of the Tensegrity Structure for Dynamic Energy and Force Distribution of Cytoskeleton during Cell Spreading. PLoS ONE 5, e14392 (2010).

20. Cramer, L. P., Siebert, M. & Mitchison, T. J. Identification of Novel Graded Polarity Actin Filament Bundles in Locomoting Heart Fibroblasts: Implications for the Generation of Motile Force. J. Cell Biol. 136, 1287–1305 (1997).

21. Pellegrin, S. & Mellor, H. Actin stress fibres. J. Cell Sci. 120, 3491–3499 (2007).

22. Riveline, D. et al. Focal Contacts as Mechanosensors. J. Cell Biol. 153, 1175–1186 (2001).

23. Misteli, T. The Self-Organizing Genome: Principles of Genome Architecture and Function. Cell 183, 28–45 (2020).

24. Uhler, C. & Shivashankar, G. V. Regulation of genome organization and gene expression by nuclear mechanotransduction. Nat. Rev. Mol. Cell Biol. 18, 717–727 (2017).

25. Starr, D. A. & Fridolfsson, H. N. Interactions Between Nuclei and the Cytoskeleton Are Mediated by SUN-KASH Nuclear-Envelope Bridges. Annu. Rev. Cell Dev. Biol. 26, 421–444 (2010).

26. Lombardi, M. L. et al. The Interaction between Nesprins and Sun Proteins at the Nuclear Envelope Is Critical for Force Transmission between the Nucleus and Cytoskeleton. J. Biol. Chem. 286, 26743–26753 (2011).

27. Mammoto, A., Mammoto, T. & Ingber, D. E. Mechanosensitive mechanisms in transcriptional regulation. J. Cell Sci. jcs.093005 (2012) doi:10.1242/jcs.093005.

28. Di, X. et al. Cellular mechanotransduction in health and diseases: from molecular mechanism to therapeutic targets. Signal Transduct. Target. Ther. 8, 282 (2023).

29. Jaroch, K., Jaroch, A. & Bojko, B. Cell cultures in drug discovery and development: The need of reliable in vitro-in vivo extrapolation for pharmacodynamics and pharmacokinetics assessment. J. Pharm. Biomed. Anal. 147, 297–312 (2018).

30. Kitaeva, K. V., Rutland, C. S., Rizvanov, A. A. & Solovyeva, V. V. Cell Culture Based in vitro Test Systems for Anticancer Drug Screening. Front. Bioeng. Biotechnol. 8, 322 (2020).

31. Wu, S. et al. Quantification of cell viability and rapid screening anti-cancer drug utilizing nanomechanical fluctuation. Biosens. Bioelectron. 77, 164–173 (2016).

Chapter 2

Tools for cell mechanical stimulation: state of art

2.1 Passive and active cell mechanical stimulation

The investigation of the dynamic interplay between cells and biophysical cues of ECM is crucial to understand the mechanisms regulating cell behavior, as well as the tissue development, regeneration, and repair[1]. Given the *in vivo* complexity, over the past few decades, multidisciplinary collaboration among the fields of biology, materials science, and biomedical engineering, has delivered expertise and advanced tools that enable *in vitro* cell mechanical stimulation, while monitoring the biological response.

Ricca et al.[2] recently proposed a new way to classify cellular mechanical stimulation , introducing the concept of "passive" and "active" inputs. Passive inputs are physical properties of the microenvironment perceived by cells, such as substrate stiffness, matrix alignment, and adhesive affinity. In contrast, active inputs regard stimuli that act directly upon the cell and include externally applied forces, displacements, and fluid shear stresses. Even if they can exploit different cell mechanosensing and mechanotransduction pathways, both active and passive stimuli share the ability to induce active biological outputs in cytoskeleton remodelling[3], biochemical signalling[4], and gene expression[5], with an impact on multiple cell functions.

In the following paragraphs of this chapter, it is then provided a review of the state of art of the biomaterials and devices for delivering passive and active mechanical stimulation to cells, focusing the attention on their design principles, stimulation approaches, and existing challenges.

2.2 Tools for passive cell mechanical stimulation

2.2.1 Biomaterials with tunable stiffness

ECM properties of tissues and organs that cells inhabit can be dramatically different from each other. Soft tissues like the brain, liver, and kidney exhibit low elastic moduli (below 10 kPa), while skeletal tissues such as bone and tooth are extremely stiff, with elastic moduli reaching tens of gigapascals. These differences in mechanical properties of these tissues and organs are largely attributed to their diverse ECM composition and structure.

Aiming to investigate how ECM stiffness modulates cellular behavior, many studies have been carried out in the past two decades by using substrates with different elastic modulus, such as (hydro)gels. Compared to many other materials, (hydro)gels are particularly interesting due to their highly programmable elastic modulus, ranging from kilopascals to hundreds of megapascals. The gels can be made of either natural polymers such as collagen, hyaluronic acid, and gelatin, or from synthetic polymers including polyacrylamide and polyethylene glycol (PEG). Modulating the stiffness of these gels is commonly achieved by controlling the precursor concentration[6]. Low precursor concentrations result in loose crosslinked networks and soft materials, while high precursor concentrations lead to denser crosslinked networks with higher stiffness. For materials that crosslink upon exposure to light (e.g., ultraviolet [UV]), the gel's stiffness can also be adjusted by changing the exposure time[7]. Application of external stimuli such as pH and temperature has been demonstrated as another effective way to alter gel stiffness. It is worth noting that although several methods exist to modulate the (hydro)gels' stiffness[8,9]; these methods not only change the stiffness of (hydro)gels, but also influence their microstructure and/or chemical composition and are therefore not commonly used.

Exploiting the versatility of these materials, several studies have shown that substrate stiffness can induce a variety of cellular responses. Pelham Jr, R. J. & Wang, Y.[10] have observed how cells cultivated on collagen-coated polyacrylamide gels display different adhesion patterns in response to the mechanical stiffness of the substrate. In particular, rigid gel promotes mature and stable focal adhesions with more structured actin filaments, while soft gel results in shorter and more dynamic complexes with a weakly assembled cytoskeleton. The different effects of substrate stiffness on cell mechanosensing elements have a direct influence on cell functions, in fact cells have higher proliferation rates on stiff gel and migrate faster on soft one. Adam Engler et al.[11] have demonstrated that ECM elasticity is also able to selectively induce the differentiation of stem cells into the specific lineage. Mesenchymal stem cells cultured on two-dimensional substrates with elastic modulus approaching the elasticity of native tissues such as brain (E ~ 0.1-1 kPa), muscle (E ~ 8-17 kPa) and bones (E ~ 40 kPa), underwent neurogenesis, myogenesis and osteogenesis, respectively. Another example is given by Evans et al.'s work in which they tested how substrate stiffness can influence embryonic stem cells (ESCs)

differentiation by growing cells on flexible polydimethylsiloxane (PDMS) substrates. Indeed, the PDMS elastomer is widely used for biomedical applications due to its numerous advantages, such as bio-compatibility, flexibility, stability over a wide range of temperatures, gas permeability, and optical transparency. Moreover, the elastic modulus of PDMS can be controlled by cross-linker concentration and/or baking time. Evans et al. cultivated ESCs on PDMS substrates of varying stiffness (0.041, 0.26, 1.9, 2.3, 2.7 MPa) and observed that cell spreading and cell growth were all increased as a function of substrate stiffness. Similarly, several genes implicated in early mesendoderm differentiation were upregulated in cell cultures on stiffer compared to softer substrates[12].

2.2.2 Biomaterials with topographical features

In addition to the substrate stiffness, cells can sense and respond to a variety of topographical signals of the ECM. Cellular sensing of these topographical features modulates cell adhesion and morphology, influencing related cell functions.

The ability to regulate cell behavior and ECM organization through topographical cues has been employed in biomaterials design for regenerative medicine applications. Various advanced fabrication technologies and material synthesis methods have been used to develop a range of topographical patterns including gratings, grooves, waves, grids, pillar arrays and nano/microscale predesigned patterns. These techniques are typically classified based on the fabrication technique and include lithography, electrospinning, laser ablation and chemical processing[13].

Such structured surfaces can be effective in controlling cell confinement and mainly the formation and growth of FAs. Different proteins adsorbed on the topographical pattern result in the formation of areas (such as ridge or pillar tops) easily accessible for FA formation, and areas (recesses such as grooves or pits) where the protrusion of the cell membrane cannot penetrate and then FAs cannot form. To facilitate appropriate cell confinement, topographic patterns must be designed with dimensions comparable to those of cells (tens of microns). Micrometric patterns influence cell confinement, but do not allow precise control over FA formation and growth. In contrast, submicrometric patterns confine the growth of FAs and limit their formation to the accessible parts of the topographies, i.e. on the pillar top, in the inter-pit area or on the grid ridges. It is important to note that the accessibility/inaccessibility of certain

material regions to cell membrane protrusions are not universal parameters but depend on the shape and size of the topographic feature (**Fig. 2.1**).

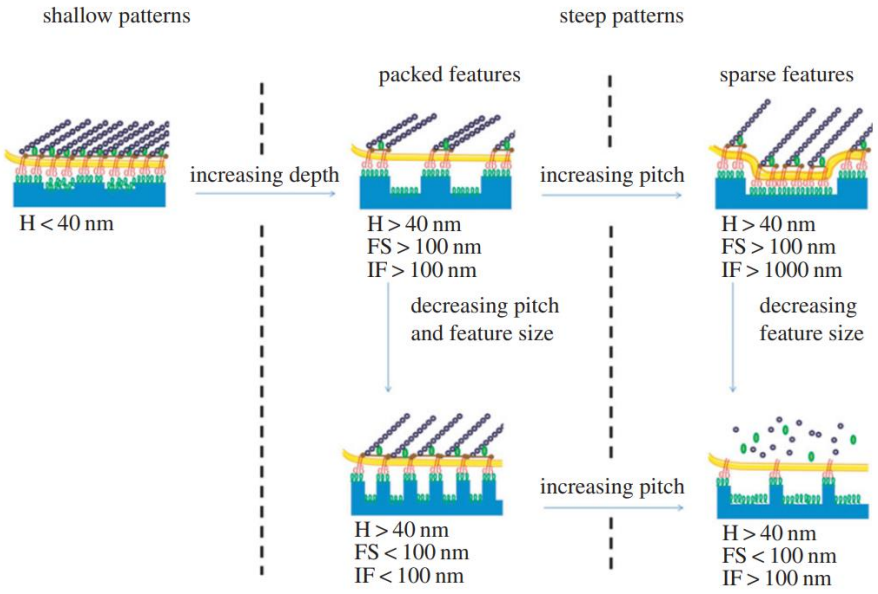

Fig. 2.1: *Illustration of cell–nanotopography interactions[38]. Different combinations of feature sizes and depths might reduce the surface available for the cell membrane to establish adhesions. Surfaces are generally coated with serum proteins, which account for a macromolecular layer of 20 –30 nm. Therefore, in order to make a surface not available for the establishment of cell adhesions, this has to be at least 40 nm away from the cell membrane. Looking at the pattern from the cell side, five integrins are necessary to connect the cytoskeleton to the extracellular environment, which requires integrin clusters of approximately 40 nm. Therefore, topographic features exceeding this dimension can be recognized by cells as 'adhesive'. From the material side, ligand spacings below 60 nm proved to be sufficient to ensure cell-substrate binding.*

In a recent study, MC3T3 preosteoblasts cultivated on nanograted PDMS substrates aligned along the nanopattern direction already at 4 h after seeding[14]. Directional growth of FAs strongly affected cytoskeleton assembly as actin fibers were aligned parallel to the pattern direction. This caused the whole cell body to assume an elongated morphology and migrate along the pattern direction, a phenomenon usually referred to as 'contact guidance'. Cell parallel alignment along nanopattern direction was found to be function of ridge/groove critical dimensions and cell type[15]. Moreover, a prior study suggested that groove depth plays a central role in cell sensitivity to nanotopographic ridges[16].

There is multiple evidence that adhesion-mediated signaling pathways are responsible for also regulating cell differentiation. In particular, Biggs et al.[17] observed reduced adhesion maturation and spreading of osteoprogenitor cells cultivated on nano-pit arrays, correlated with impaired osteospecific differentiation. Moreover, these stimuli can also have a significant impact on how the cells produce and organize the natural ECM. For example, electrospun nanofibrous and

nanopatterned substrates have been shown to direct the formation of highly aligned collagen fibers by different cell types[18–20].

2.3 Tools for active cell mechanical stimulation

2.3.1 Atomic force microscopy

Atomic force microscopy (AFM) technique was originally developed as a tool for nanoscale imaging of the topography of solid substrates, but it has progressively emerged as a key tool for mapping the mechanical properties of living biological samples. In particular, AFM can be used to apply a controlled amount of force, ranging from pico to nanonewton, on spatially defined areas of the cell membrane.

Briefly, in AFM, a cantilever with a tip at one end is used to probe the cell (**Fig. 2.2 A**). The displacement in the z direction of the cantilever is measured using a laser that reflects off the back surface of the cantilever beam. If the spring constant of the cantilever is softer than the surface being probed, the cantilever bends and the deflection is measured using a position sensitive detector. The force-indentation curve, defined as the applied force vs. the distance of the tip from the sample surface, is often fitted to a Hertz model of contact mechanics (**Fig 2.2 B**).

The employment of cantilevers with a spherical tip protects the cells against potential damage during force application and enables the use of AFM as a local indenter[21]. This configuration was exploited by Elosegui-Artola et al.[22] to indent the nucleus of fibroblasts. Their work highlighted that forces exerted on the nucleus result in the nuclear translocation of the transcription factor YAP.

AFM has been exploited as a research tool by the biophysics community because this technique affords high imaging resolution, positioning accuracy and the ability to mechanically manipulate biological structures and molecules. However, one of the main disadvantages of AFM is that the applied force depends on the shape of the AFM tip and the location of the indentation and, therefore, results are not easily transferable between experiments. Another major issue is represented by the maintenance of cellular viability, considering the difficulties of controlling the sample environment with the AFM instrumentation in place.

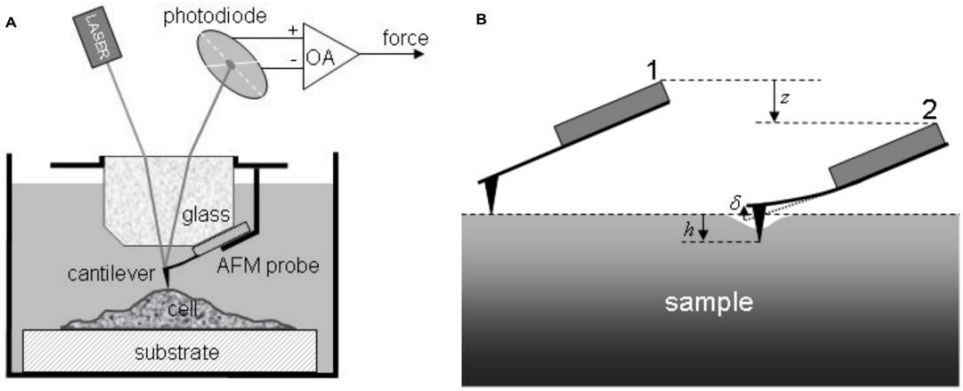

Fig. 2.2: *AFM technique for cell indentation[39]. (A) Sketch of the AFM setup used for study of living cells in physiologic medium. The liquid cell is fixed and contains the sample and the measurement medium, while the AFM probe is moved by the AFM scanner. The laser beam reflected by the cantilever of the AFM probe is used for the force detection. (B) Sketch illustrating the relationship between vertical displacements of the AFM probe (z) and tip (h) and the deflection of the cantilever (δ). The arrows indicate the positive direction of the displacements.*

2.3.2 Optical tweezers

Optical-mechanical systems employ photon trapping to manipulate and apply forces to whole cells, or a portion of a cell. This technique uses an infrared laser and a microscope to trap a nano or micron sized object, typically a transparent bead, and control its movements through a highly focused laser beam. The laser beam is focused on the center of the object and when the photons of the laser beam pass through the bead, there is a change in their direction based upon the object's refractive index. This results in a transfer of momentum to the bead. Imbalances in intensity between the center and the outside of the beam cause a net force on the bead acting towards the higher intensity part, thus moving the bead towards the center of the beam. When the beam moves, the bead is held in its center, as in a pair of tweezers.

Forces produced by optical tweezers are on the order of 0.1–100 piconewtons, which makes it ideal for cellular and molecular level force probe applications. In particular, optical techniques have been used to investigate single cell mechanics, by controlled displacement of dielectric objects that are either attached to the cell membrane or placed inside the cell. An oscillatory optical trap has been used to apply forces to the cell membrane in the piconewton range. This mechanical stimulation induced a local membrane indentation and cellular calcium transients, which were observed to be dependent on the stimulus strength and the force pulse frequency[23] (**Fig. 2.3**).

The main disadvantages of the optical-mechanical techniques are the damage and heat they

induce in the sample, as well as the relatively low forces that can be applied.

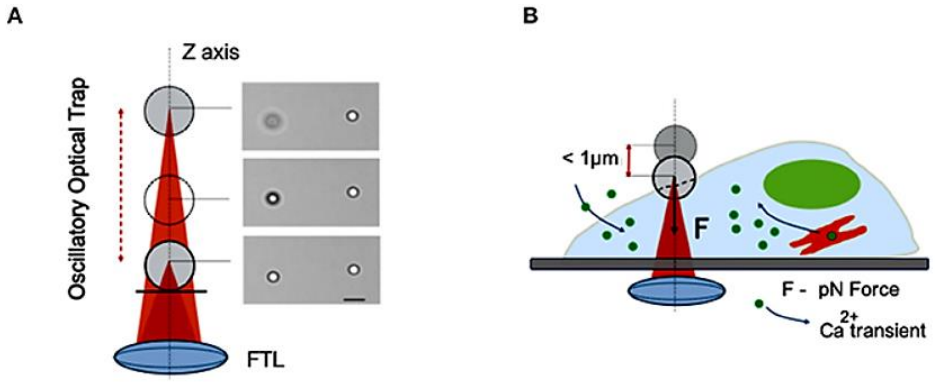

Fig. 2.3: *Overview of the mechanical stimulation with piconewton forces by optical tweezers[22]. (A) The Oscillatory Optical Trap (OOT), implemented with a Focused Tunable Lens (FTL), enables continuous movement of the trap along the z-axis. (B) Scheme of the mechanical stimulation inducing calcium transient experiment.*

2.3.3 Magnetic tweezers

Magnetic tweezers rely on the manipulation of paramagnetic beads by applying a controlled magnetic field that exerts pulling forces on the beads. The bead's movement is manipulated by a magnetic field produced by an electromagnetic coil probe in proximity to the bead, the magnitude of the force applied to the bead depends on the magnetic field and the proximity to the sample (**Fig. 2.4**). The applications of these techniques are very similar to optical tweezers, and they can be used for almost any cell type, within most materials and media types. They have the added advantage that the majority of cells and media fluids have relatively small magnetic susceptibility and compared to optical techniques, this prevents sample damage by illumination or heat.

Paramagnetic beads can be chemically functionalized to present adhesion proteins at their surface that can be recognized by the cell cytoskeleton. Recently, Tajik et al.[24] applied precisely controlled oscillating forces to magnetic beads attached to individual cells. The authors demonstrate that external forces are transmitted to the nucleus, leading to chromatin stretching and changes in gene transcription.

One of the limitations of this magnetic tweezer technique is that when micron sized beads are inserted into the cytoplasm, the presence of an external object can be destructive to the cell and undefined interactions of the bead with the intracellular components can lead to an incorrect estimation of the mechanical properties.

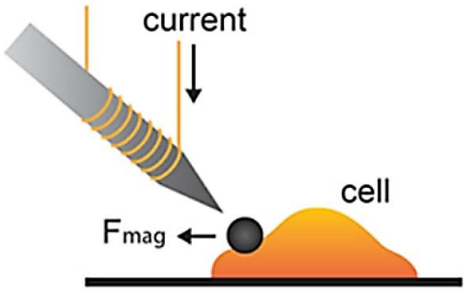

Fig. 2.4: *Schematic representation of the magnetic tweezers[40]. Superparamagnetic beads are attached to the cell. Then, a copper solenoid and a soft iron tip produce a high magnetic field gradient, creating a force F tweezers on the beads.*

2.3.4 Shear flow microfluidic devices

Physiologically, fluid flow in the body originates from both blood flow and interstitial fluid. In vitro, shear stress is applied to induce fluid flow on cells cultured as a monolayer.

To understand the influence of fluid shear, and to exert high control of the shear direction and simultaneously monitor shear-induced changes efficiently, different microfluidic flow chambers have been designed. For example, Song et al.[25] developed a multi-compartment shear flow microfluidic platform using a braille piezoelectric array of pins that functions as valves with a multi-step peristaltic pumping sequence. The channels control the shear stress by controlling the flow rate (volume displacement by the pump), which is indirectly controlled by the frequency of pumping sequence (braille pin movement). Using this setup, the authors highlighted how the microfluidic flows caused endothelial cells to align and elongate significantly in the direction of flow according to their exposed levels of shear stress.

It has to be mentioned that shear stresses perceived by cells are affected by various factors, such as cell size and motility, uniformity of cell distribution, and viscosity of the fluid, impacting experiment reproducibility.

2.3.5 Cell stretching systems

In a typical stretching experiment, cells are cultured on a thin, elastic, transparent substrate coated with extracellular matrix molecules to promote cell spreading and adhesion. Uniform

uniaxial or biaxial strain is subsequently applied to the substrate while monitoring the cellular response before, during, and after strain application. The degree of cell response depends on various factors including load direction, magnitude, and timing. This motivates the development of several cell stretching devices for better understanding of the cell response to the stretching stimulus. Even if they share the same aim, cell stretching systems are characterized by different structural and functional features including actuation principle, stretching pattern, and microscope compatibility.

Most laboratory-developed cell stretching systems are actuated using electric motors. The latter are characterized by high precision and intuitive programmability with a relatively simple setup for both static and dynamic loading but, on the other hand, the ongoing need for lubrication and the possibility for device erosion are major concerns for cell contamination.

Ursekar et al.[26] designed a mechanical equibiaxial cell stretching system based on the indenter design, using a stepper motor as actuator. The device consists of a membrane holder ring fixed to a mobile plate, where the indenter ring placed on the base is smaller than the membrane holder ring. The controlled vertical downward motion of the mobile plate leads to membrane stretching upon the indenter. Moreover, the authors addressed the issue of not homogeneous strains by fabricating a 1-mm thick and 10-mm tall cylindrical wall on the membrane to confine the cells (**Fig. 2.5 A**). Even if it has been reported to be compatible with inverted microscopy and cycling stretching, this stretching device design lacks the possibility to apply uniaxial or biaxial strains to the cells.

Another example of electromechanical cell stretcher can be found in Chang et al. work, where a translation stage was actuated for the stretching of neural stem cells[27]. In this case, the flexible stretching substrate with micropatterns was clamped with one end fixed to the base and other end connected to the translation stage. Linear motion of translation stage actuated by the motor transfers the strain to the substrate and results in the stretching. The peculiarity of this design is the use of micropatterned channels parallel and perpendicular to the direction of stretching which allow different stretching conditions to be compared simultaneously (**Fig. 2.5 B**).

Recently, more elegant techniques have been pursued commercially, such as STB-190-XY from Strex Systems for cell Stretching (STREX Inc.). Strex Inc. utilizes a PDMS-based cell culture chamber and high-precision stepper motors for a consistent range of motion at a variety of speeds and stretch ratios. The advantages of this device are the compatibility with high resolution microscopy and the possibility to apply uniaxial and biaxial stretching independently. However, the limits are represented by limited strain magnitude (20% in each direction) and continuous working time (15-20 minutes).

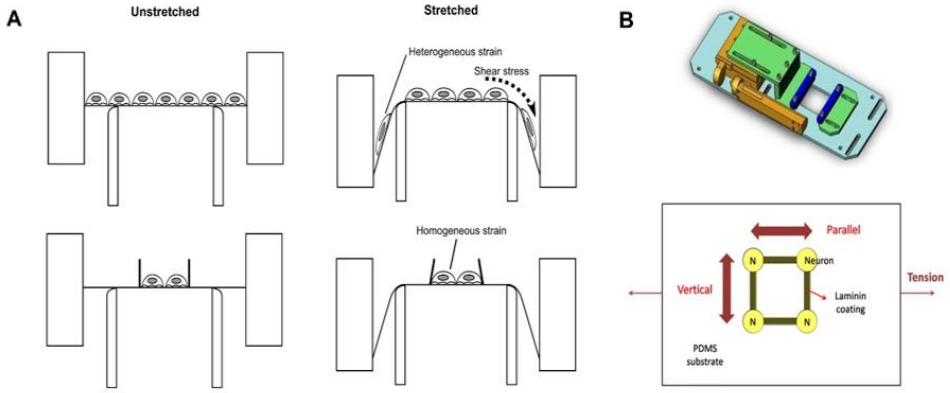

Fig. 2.5: *Examples of cell stretching devices with electromechanical actuation. (A) Comparison of strains imposed upon cells in different designs of equibiaxial stretching device when the circular clamp holding the membrane is moved downwards along the concentrically placed indenter*[25]*. (B) Schematic of the linear stage stretching system and micropatterned PDMS substrate*[26]*.*

Another diffused approach to induce stretching is the pneumatic actuation. The majority of devices using pneumatic actuation techniques are based on the deformation of a thin membrane with controlled actuation pressure. For example, Kreutzer et al.[28] developed a circular device with a thin membrane and computer controlled vacuum pressure in the cavity between the two PDMS shells to deform the membrane. This induced a symmetrical radial stress onto the inner shell and, subsequently, stretched the cells grown on the membrane. Live-cell imaging was conducted using an inverted microscope. However, applying a vacuum to the actuation chamber led to a displacement of the cell culture membrane in the z-direction. Although such out-of-plane displacement is common with pneumatic actuation of elastomeric membranes, it is rarely discussed in the literature, posing a challenge for live-cell microscopy. To address this limitation, Kreutzer et al. manually refocused between stretching cycles and utilized low-magnification objectives to minimize the impact of displacement on image quality.

Tremblay et al.[29] ingeniously employed low pressure in their device for cell stretching. The stretching system includes four low-pressure channels (red), two fluidic channels (purple and blue), and a membrane. This membrane is placed between the two fluidic channels. The upper fluidic channel is utilized for cell seeding, while the lower one compensates for the pressure generated during seeding. Application of low pressure to a designated channel deforms the vertical wall around the cell, thus delivering the stretching stimulus to them. The device can be converted between uniaxial and biaxial stretching as the forces applied to both sides of the membrane can be controlled independently.

A commercial alternative based on pneumatic actuation is produced by Flexcell International Corporation. Flexcell International's instruments. In particular, the FX-6000T is composed of a loading column whose upper surface is positioned beneath the elastic membrane's center. Based on the loading post's shape (cylindrical or rectangular), the central membrane is stretched in different ways (equibiaxially or uniaxially, respectively) by applying a vacuum to the peripheral portion of the post. The FX-6000T device has various advantages. Firstly, it can control up to 24 culture wells in parallel with the same tension system and, secondly, the computer system can precisely regulate the loading cycle, size, frequency, duration, etc. of the stretching force. Indeed, the system has high stability and can run continuously, keeping the loading waveform stable. The drawbacks, on the other hand, are related to the inability to independently control the two stretching directions and adapt this device to any microscope for live imaging.

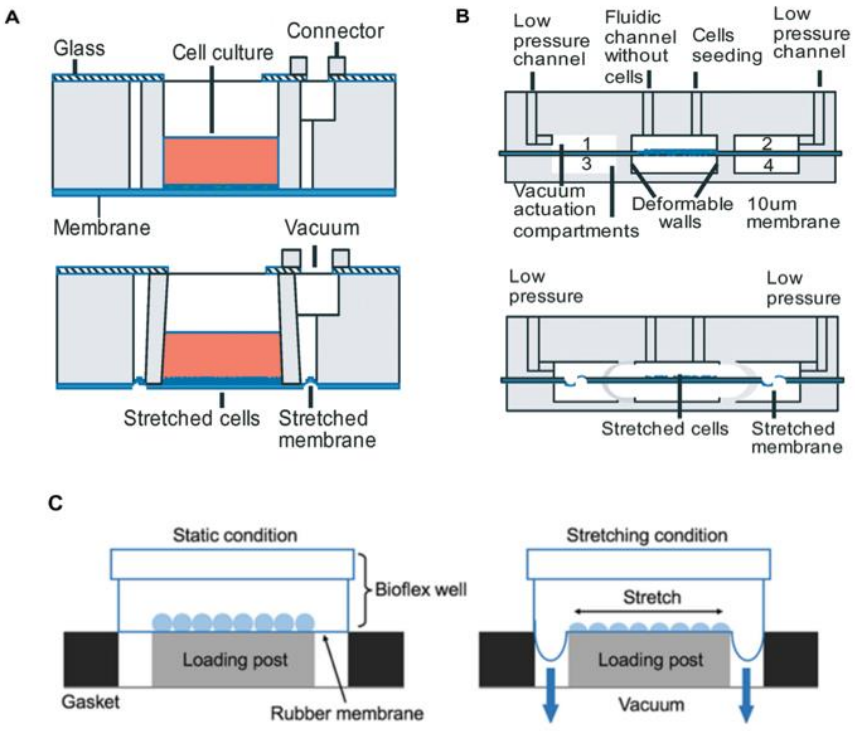

Fig. 2.6: *Examples of cell stretching devices with pneumatic actuation. (A) Side view of radial stretching with circular support and negative pressure[27]. (B) Four-chamber side actuation with negative pressure. Schematic cross-section of the device with cells attached on the membrane and low-pressure conditions[28]. (C) Schematic diagram of the FX-6000T.*

Apart from the major actuation techniques discussed above, other concepts such as piezoelectric[30], electromagnetic[31] and optical[32] actuations have also shown their potential.
The availability of these heterogeneous devices has provided a deeper understanding of the cell

mechanotransduction mechanisms in response to mechanical stretching. Depending on the strain direction, amplitude and frequency, cell cyclic stretching has been shown to be able to remodel adhesion sites and actin stress fibers, reorienting them parallel, obliquely, or perpendicularly to the main stretching direction[33]. In another work, Tsukamoto S. et all characterized the nuclear deformations induced by uniaxial stretching, underlying the role of actin cytoskeleton in transferring the strain from the substrate to the nucleus[34]. On this line, cell stretching is able to induce transcription factors shuttling inside the nucleus[21] and alterations of chromatin condensation and gene expression levels[35].

2.4 References

1. Discher, D. E., Mooney, D. J. & Zandstra, P. W. Growth Factors, Matrices, and Forces Combine and Control Stem Cells. Science 324, 1673–1677 (2009).

2. Ricca, B. L., Venugopalan, G. & Fletcher, D. A. To pull or be pulled: parsing the multiple modes of mechanotransduction. Curr. Opin. Cell Biol. 25, 558–564 (2013).

3. Shao, Y. et al. Uniaxial cell stretching device for live-cell imaging of mechanosensitive cellular functions. Rev. Sci. Instrum. 84, 114304 (2013).

4. Liu, B. et al. RhoA and Membrane Fluidity Mediates the Spatially Polarized Src/FAK Activation in Response to Shear Stress. Sci. Rep. 4, 7008 (2014).

5. Harper, C. E. et al. Mechanical stimuli activate gene expression via a cell envelope stress sensing pathway. Sci. Rep. 13, 13979 (2023).

6. Jin, C., Wang, Z., Volinsky, A. A., Sharfeddin, A. & Gallant, N. D. Mechanical characterization of crosslinking effect in polydimethylsiloxane using nanoindentation. Polym. Test. 56, 329–336 (2016).

7. Paiva, S. et al. Polyacrylamide Hydrogels with Rigidity-Independent Surface Chemistry Show Limited Long-Term Maintenance of Pluripotency of Human Induced Pluripotent Stem Cells on Soft Substrates. ACS Biomater. Sci. Eng. 6, 340–351 (2020).

8. Huang, Y. et al. Energy-Dissipative Matrices Enable Synergistic Toughening in Fiber Reinforced Soft Composites. Adv. Funct. Mater. 27, 1605350 (2017).

9. Hua, M. et al. Strong tough hydrogels via the synergy of freeze-casting and salting out. Nature 590, 594–599 (2021).

10. Pelham, R. J. & Wang, Y. Cell locomotion and focal adhesions are regulated by substrate flexibility. Proc. Natl. Acad. Sci. 94, 13661–13665 (1997).

11. Engler, A. J., Sen, S., Sweeney, H. L. & Discher, D. E. Matrix Elasticity Directs Stem Cell Lineage Specification. Cell 126, 677–689 (2006).

12. Dept Materials, Royal School of Mines, Imperial College, Prince Consort Road, London SW7 2BP, U.K. et al. Substrate stiffness affects early differentiation events in embryonic stem cells. Eur. Cell. Mater. 18, 1–14 (2009).

13. Zhang, Y. & Habibovic, P. Delivering Mechanical Stimulation to Cells: State of the Art in Materials and Devices Design. Adv. Mater. 34, 2110267 (2022).

14. Natale, C. F., Ventre, M. & Netti, P. A. Tuning the material-cytoskeleton crosstalk via nanoconfinement of focal adhesions. Biomaterials 35, 2743–2751 (2014).

15. Lamers, E. et al. The influence of nanoscale grooved substrates on osteoblast behavior and extracellular matrix deposition. Biomaterials 31, 3307–3316 (2010).

16. Teixeira, A. I., Abrams, G. A., Bertics, P. J., Murphy, C. J. & Nealey, P. F. Epithelial contact guidance on well-defined micro- and nanostructured substrates. J. Cell Sci. 116, 1881–1892 (2003).

17. Biggs, M. J. P. et al. The use of nanoscale topography to modulate the dynamics of adhesion formation in primary osteoblasts and ERK/MAPK signalling in STRO-1+ enriched skeletal stem cells. Biomaterials 30, 5094–5103 (2009).

18. Xing, Q., Vogt, C., Leong, K. W. & Zhao, F. Highly Aligned Nanofibrous Scaffold Derived from Decellularized Human Fibroblasts. Adv. Funct. Mater. 24, 3027–3035 (2014).

19. Su, Y. et al. 3D Electrospun Synthetic Extracellular Matrix for Tissue Regeneration. Small Sci. 1, 2100003 (2021).

20. Wu, S., Wang, Y., Streubel, P. N. & Duan, B. Living nanofiber yarn-based woven biotextiles for tendon tissue engineering using cell tri-culture and mechanical stimulation. Acta Biomater. 62, 102–115 (2017).

21. Charras, G. T. & Horton, M. A. Single Cell Mechanotransduction and Its Modulation Analyzed by Atomic Force Microscope Indentation. Biophys. J. 82, 2970–2981 (2002).

22. Elosegui-Artola, A. et al. Force Triggers YAP Nuclear Entry by Regulating Transport across Nuclear Pores. Cell 171, 1397-1410.e14 (2017).

23. Falleroni, F., Torre, V. & Cojoc, D. Cell Mechanotransduction with Piconewton Forces Applied by Optical Tweezers. Front. Cell. Neurosci. 12, 130 (2018).

24. Tajik, A. et al. Transcription upregulation via force-induced direct stretching of chromatin. Nat. Mater. 15, 1287–1296 (2016).

25. Song, J. W. et al. Computer-Controlled Microcirculatory Support System for Endothelial Cell Culture and Shearing. Anal. Chem. 77, 3993–3999 (2005).

26. Ursekar, C. P. et al. Design and Construction of an Equibiaxial Cell Stretching System That Is Improved for Biochemical Analysis. PLoS ONE 9, e90665 (2014).

27. Chang, Y.-J., Tsai, C.-J., Tseng, F.-G., Chen, T.-J. & Wang, T.-W. Micropatterned stretching system for the investigation of mechanical tension on neural stem cells behavior. Nanomedicine Nanotechnol. Biol. Med. 9, 345–355 (2013).

28. Kreutzer, J. et al. Pneumatic cell stretching system for cardiac differentiation and culture. Med. Eng. Phys. 36, 496–501 (2014).

29. Tremblay, D., Chagnon-Lessard, S., Mirzaei, M., Pelling, A. E. & Godin, M. A microscale anisotropic biaxial cell stretching device for applications in mechanobiology. Biotechnol. Lett. 36, 657–665 (2014).

30. Kamotani, Y. et al. Individually programmable cell stretching microwell arrays actuated by a Braille display. Biomaterials 29, 2646–2655 (2008).

31. Kamble, H. et al. An Electromagnetically Actuated Double-Sided Cell-Stretching Device for Mechanobiology Research. Micromachines 8, 256 (2017).

32. Sraj, I. et al. Cell deformation cytometry using diode-bar optical stretchers. J. Biomed. Opt. 15, 1 (2010).

33. Giverso, C., Loy, N., Lucci, G. & Preziosi, L. Cell orientation under stretch: A review of experimental findings and mathematical modelling. J. Theor. Biol. 572, 111564 (2023).

34. Tsukamoto, S. et al. Compressive forces driven by lateral actin fibers are a key to the nuclear deformation under uniaxial cell-substrate stretching. Biochem. Biophys. Res. Commun. 597, 37–43 (2022).

35. Nava, M. M. et al. Heterochromatin-Driven Nuclear Softening Protects the Genome against Mechanical Stress-Induced Damage. Cell 181, 800-817.e22 (2020).

Chapter 3

Realization of a cell stretching system for the administration of mechanical doses to cells

3.1 Introduction

The understanding of cell mechanobiological response requires advanced tools for the in vitro administration of mechanical signals to cells.

Among the different techniques illustrated in the previous chapter, cell stretching has been selected for the purposes of this project. In fact, cell stretching technique offers a precise control over the applied mechanical force, with the possibility to easily modulate its magnitude, direction, and frequency. Moreover, compared to micropipette aspiration and AFM techniques that mechanically stimulate cells one by one, stretching experiments allow simultaneously probing of many cells at once. This provides a more comprehensive view of the collective cellular response under conditions that closely resemble physiological conditions. For example, mechanical stretching helps mimic mechanical forces experienced by muscle and cardiovascular cells, aiding in the development of engineered and functional tissues[1,2]. Studying cell mechanical properties, including stiffness, viscoelasticity, and response to dynamic forces, under controlled stretching conditions also enhances our understanding of tissue biomechanics, with possible applications in wound healing and regenerative medicine fields[3].

A number of these studies has been conducted using commercially available stretching devices (e.g., Flexcell and STREX Inc.), which are identified by well-characterized strain profile, homogeneous strain pattern and adaptability of stretching modes. These systems, however, are often expensive (> 20,000 €), hard to customize and have limited functional capabilities, since they are built to work in a specific range of stimulation parameters.

In this project it is reported the development of a highly flexible custom-made cell stretching system, capable of administering spatially and temporally precision-controlled mechanical stimuli to cells. The compatibility with live-cell imaging allows the real-time monitoring of cell response. Moreover,

the main novelty of this device lies in the ability to standardize the cell perception of the stretching stimulus through topographical cues, in a way to foster a coherent cell biological response.

The different phases of project's design, realization, and characterization are described in the following sections of this chapter, highlighting the main features of this powerful device.

3.2 Materials and methods

3.2.1 Cell stretcher hardware components

The base of the cell stretcher, which provides mechanical support function and microscope mountability, was realized in plexiglass. Six 4 mm diameter holes corresponding to the threaded holes of the microscope stage enabled the adaptability to the ZEISS Axio Observer Z1 inverted microscope. However, additional holes were realized to fit with the stage of ZEISS LSM700 inverted confocal microscope.

On top of the base, the cell stretcher was made up of a combination of 3D printed and mechanical components. In particular, prisms and joints (coupled to the bearings and the lead screws, respectively) were 3D printed through Asiga max X27 with Freeprint ortho resin. The standard hardware components, instead, included stainless steel trapezoidal reverse screws, lead screws, linear rods, mechanical joints and bearings, pulley, belt, and motor holders.

Regarding the actuation system, the motors selected were SanyoDenky 103-H7123-5040 stepper motors, connected to DM542 drivers and controlled through Arduino Mega.

3.2.2 Nanopattern membrane fabrication

The fabrication of nanopatterned membranes was achieved by means of a replica molding process. In particular, both master and membranes were made in polydimethylsiloxane (PDMS) (Sylgard 184, Dow Corning Corporation, Michigan, USA), by mixing elastomer base and curing agent at 10:1 weight ratio and degassing the solution under vacuum for 1 h.

Firstly, PDMS masters were obtained through replica molding technique from a master (**Fig. 3.1 A**) fabricated by means of two-photon polymerization (2PP) technique using the 3D

printing Nanoscribe Photonic Professional GT System (Nanoscribe GmbH). This instrument uses a 780 nm Ti-sapphire laser emitting ≈ 100 fs pulsed at 80 MHz with a maximum power of 150 nW and it is equipped with 63x oil immersion objective (1.4 N.A.). A specific photoresist called Ip-Dip (Nanoscribe GmbH) was used to accurately fabricate structures with submicrometric resolutions. More specifically, the master consisted of an area of 15 × 15 mm^2 made of parallel nanogrooves with a groove and ridge width of 700 nm and depth of 350 nm. These structures were fabricated on 25 × 25 mm^2 fused silica substrates (3D SF DiLL - Nanoscribe GmbH). Starting from the fabricated nanopatterns in Ip-Dip, using the replica molding technique, specific PDMS nanopatterned masters were obtained. In order to finely replicate the nanometric features, the PDMS was poured on the master, degassed to remove air bubbles, and cured at 130 °C for 20 min. After cooling, a peeling off of the PDMS membrane from the Ip-Dip master was done.

In order to employ PDMS replica as master, surfaces were firstly activated with oxygen plasma (50 W, 60 s) and subsequently silanized with 500 ul of fluorolink solution (94% isopropyl alcohol, 4% double distilled water, 1% acetic acid, 1% fluorolink) spin-coated on each master surface at 3000 rpm for 60 s. After that, PDMS masters were placed in the oven at 100 °C for 1 h. Then, PDMS masters were thoroughly washed in ethanol and, then, dried at room temperature overnight. Finally, 100 µm thick PDMS nanopatterned membranes were obtained by spin-coating PDMS onto the masters at 1000 rpm for 1 min and they were cured in the oven at 130 °C for 20 min (**Fig. 3.1 B**).

SEM (Scanning Electron Microscope, S-4800 model, Hitachi, Krefeld, Germany) images were used to ensure the correct replication of nanopatterned features on PDMS masters and membranes (**Fig. 3.1 C**).

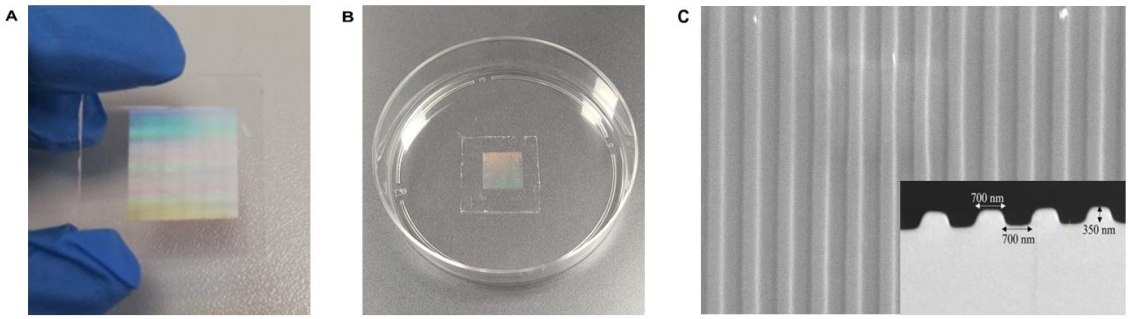

Fig. 3.1: *PDMS nanopatterned membrane fabrication. (A) Silica master. (B) PDMS nanopatterned membrane. (C) SEM images for nanopattern features quantification.*

3.2.3 Cell chamber realization

The PDMS cell chamber measured 49 × 49 × 7 mm^3 with a 35 × 15 mm^2 rectangular feature at the center. It was fabricated through the attachment of a chamber well to the nanopatterned membrane. Chamber well was realized by pouring PDMS into a 3D printed replying master (3D printer Stratasys Object 30) (**Fig. 3.2 A**). After curing at 80 °C for 2 h, the PDMS chamber well was subsequently taken away from the master and attached to the nanopatterned membrane. The bonding was realized using uncured PDMS as an adhesive glue of the base of the chamber well and the nanopatterned membrane and curing again the assembled cell chamber at 80 °C for 2 h (**Fig. 3.2 B**).

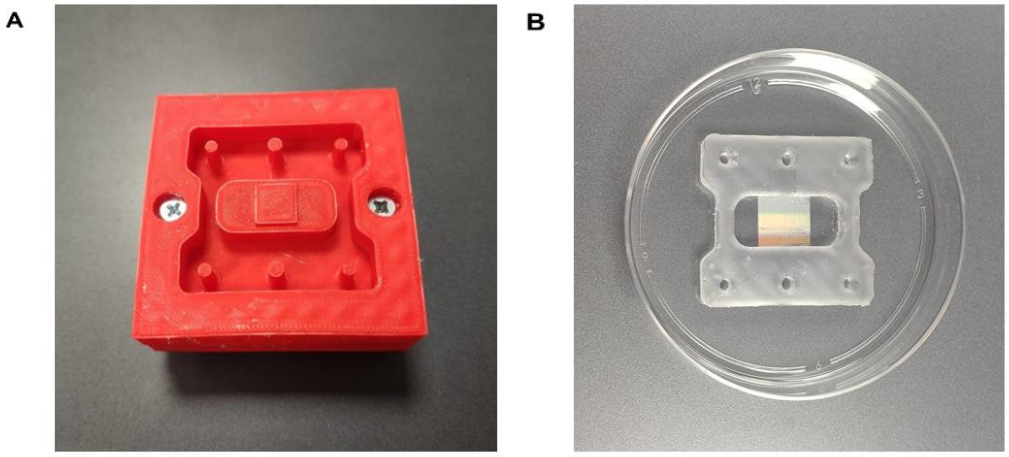

Fig. 3.2: *Cell chamber realization. (A) 3D printed chamber mold. (B) PDMS cell chamber realized through the bonding of chamber wall and nanopatterned membrane.*

3.2.4 Finite element analysis

The PDMS cell chamber was modeled as a 3D deformable solid using commercial software Abaqus 6.13.1 (SIMULIA, Dassault Systèmes). The PDMS was modeled as a neo-Hookean hyperelastic and isotropic material with Poisson ratio of 0.42 and Young's modulus of 2.5 MPa. The 30% strain on the y-axis of the cell culture region was achieved by the symmetrical application of a 2.65 mm displacement to the chamber holes in the y direction (**Fig. 3.3 A, B**). In order to accurately simulate the stretching of cell chamber by means of the bolts, the cylindrical faces of the chamber holes were divided into two sections respect the plane perpendicular to the stretching direction and the displacement was applied only to the sections

which actually undergoes the bolts traction during stretching. Eventually, x-directional as well as y-directional logarithmic strain fields were generated. Since the cell culture region was strained by 30% uniaxially, the uniform strain field was defined as 30% ± 1.5% strain area, while an error of ± 0.2% was considered in the transverse direction (where a negative 3.5% of strain was detected). The percentage area ratio of uniform strain fields was computed with respect to the total area of the cell culture region. In order to evaluate the nanopattern features changes upon stretching, a small piece (14.7 × 14.7 μm^2 of 100 µm depth) of nanopatterned membrane in the uniform strain field was modeled as already said in Abaqus software. A 30% strain in the y direction (nanopattern direction) was achieved through 2.205 µm wall symmetrical displacement (**Fig. 3.3 C**). Then, the nanopattern strain fields were generated.

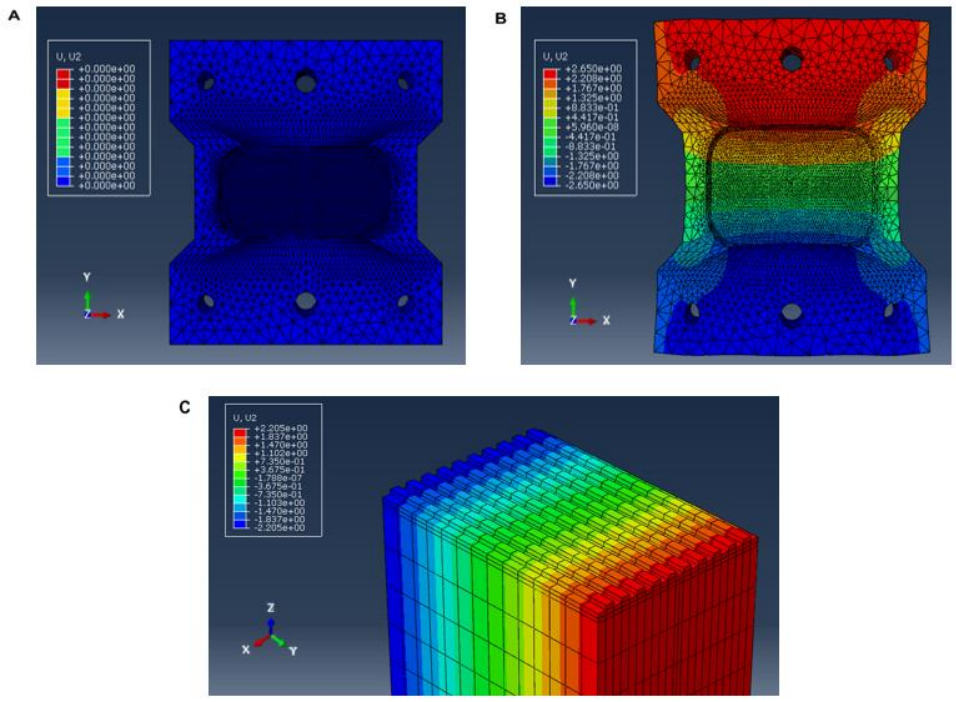

Fig. 3.3: *Finite element analysis (FEA) of cell chamber and nanopattern stretching. (A) Cell chamber in relaxed conditions (no stretch). (B) Uniaxial cell chamber stretching in y direction in order to achieve the 30% strain of the cell culture region. (C) Uniaxial 30% strain of nanopatterned substrate.*

3.2.5 Cell culture

Mouse embryo fibroblasts NIH3T3 cell line has been cultured at 37°C in 5% CO2 in humidified incubator in Dulbecco's modified Eagle's (DMEM) high glucose medium (Sigma-Aldrich, D5671) supplemented with 10% bovine calf serum (Sigma-Aldrich, C8056), 1% L-glutamine

(Sigma, St. Louis, MO), and 1% sodium pyruvate (ThermoFisher).
Prior to cells seeding, cell stretching chamber was sterilized by ultraviolet exposure for 1 h and, then, chamber culture surface was incubated with 50 ug/ml of human fibronectin for 1 h at 37 °C. At the end of coating procedure, cells were seeded at a density of $1 \cdot 10^3$ cells/cm^2 and left to adhere for 24 h in the incubator. The day after, for live experiments, 2 ml of cell medium were supplemented with 25 mM HEPES (ThermoFisher) and the cell chamber was mounted on the cell stretcher device.

3.2.6 Immunological staining

Cell cytoskeletons, nuclei and FAs were examined by immunofluorescence confocal microscopy to evaluate their orientation on nanopatterned substrate.
After 24 hours of culturing, cells have been fixed in 4% paraformaldehyde in phosphate-buffered saline 1X (PBS) (Sigma-Aldrich) for 20 min, rinsed twice with PBS and permeabilized in 0.1% Triton X-100 in PBS for 10 min. Cells have been washed three times with PBS and blocked for 1 h in 3% bovine serum albumin (BSA, Sigma-Aldrich) in PBS to block nonspecific binding. After washing two times with PBS, cells have been incubated for 1 h with the primary antibody, RabMab rabbit mAb clone: Y113 to Pa, at 1:250 dilution in PBS-BSA. Then, cells have been washed for other three times with PBS-BSA and incubated for 30 min with the secondary antibody, Alexa 546 anti-rabbit, at 1:1000 dilution and Alexa 488 phalloidin at 1:200 dilution in PBS-BSA. Cell nuclei were stained with Hoechst 33342 (1:10,000 in PBS) for 20 min. Finally, cells have been washed three times with PBS-BSA.
Images were collected with the confocal microscope (LSM700 ZEISS) with 63x oil immersion objective.

3.2.7 Orientation analysis

Cells, nuclei, and FAs polarization was assessed using Fiji software through the projection of z-stack images. Cells and nuclei orientation was determined from phalloidin and Hoechst 33342 staining, respectively. Cell and nuclei images were first converted to binarized masks representative of their shapes using appropriate threshold selected manually. Then the Fit

Ellipse function in Fiji was used to determine the minimal ellipse that encompasses the binarized images. The angle between the ellipse primary axis and a line parallel to the x-axis of the images was defined as cells and nuclei orientation.

FAs orientation was measured following a modified procedure of the one proposed by Maruoka et al.[4]. In particular, digital images of FAs were firstly processed using blur command and then subtracted from the original images using the image calculator command. The images were further processed with threshold command to obtain binarized images. Finally, particle analysis was performed in order to determine the morphometric descriptors, from which FAs orientation was extracted. Only FAs whose area was above 1 μm^2 were included in the analysis. During the orientation analysis of all the cellular components, nanopattern direction was defined as 0°. For this reason, 90° was subtracted from each angle extracted from the images to report the orientation in the range [-90°, 90°]. Finally, the percentages of cells, nuclei, and FAs that fall within the 10° increment intervals were counted.

3.2.8 Optimization of environmental conditions for live cell experiments

Live cell experiments were performed after 24 h of culturing. Cell nuclei were stained with Hoechst 33342 (1:10,000 in culture medium) for 20 min. Then, the incubation medium was replaced with 2 ml of cell culture medium supplemented with 25 mM HEPES and the cell chamber was mounted on the cell stretcher device inside the pre-heated incubator. In relaxed chamber conditions (no stretching), cell nuclei images were acquired on Zeiss Axio Observer Z1 inverted microscope each 30 min using 63x objective. A LED intensity of 10% and an exposure time of 50 ms were set for the acquisitions in order to not induce photodamage and photobleaching to the sample. Nuclear images were converted to binarized masks using appropriate threshold selected manually in Fiji. Then, nuclear outlines were selected using the wand tool and areas were measured. The percentage area changes on the same nuclei were computed respect the nuclear area at time 0 (A_0) in the following way: $\%A_i = ((A_i - A_0) / A_0) \cdot 100$, where A_i is the nuclear area at time i.

For the optimization of environmental conditions in the microscope incubator, cell culture medium temperature inside the cell stretching chamber was measured through a probe thermometer. In particular, temperature was estimated at different time points of 1 min for 1 h

from the introduction of the cell chamber inside the pre-heated cage incubator. Regarding the pH of the medium, pH drifts were visually evaluated from the color changes of phenol red.

3.2.9 Membrane strains calibration

In order to evaluate membrane strains, drops (2 µl each) of an ethanol solution containing 1% of 1 µm diameter green fluorescent beads (ThermoFisher, 490/520 nm excitation/emission wavelength) were deposited on the uniform strain region of chamber membrane and dried at room temperature. Then, the cell chamber was filled with 2 ml of PBS to simulate the weight of cell culture medium during live cell experiments and it was mounted the cell chamber on the stretching device. Incremental lead screws displacements of 1 mm were applied and images of the obtained fluorescent marks were acquired at each step increment on ZEISS Axio Observer Z1 microscope (**Fig. 3.4**). The local strains of chamber membrane were obtained from the longitudinal and transverse strains of the marks. The latter were calculated in Fiji by manually fitting the marks outline in a rectangle and measuring the length (L_i) of its sides after stretching. Then, the engineering strains were calculated respect the initial lengths (L_o) of the marks in unstretched condition: $\varepsilon_i = ((L_i - L_o) / L_o) \cdot 100$. The calibration of membrane strains was performed on three different cell chambers.

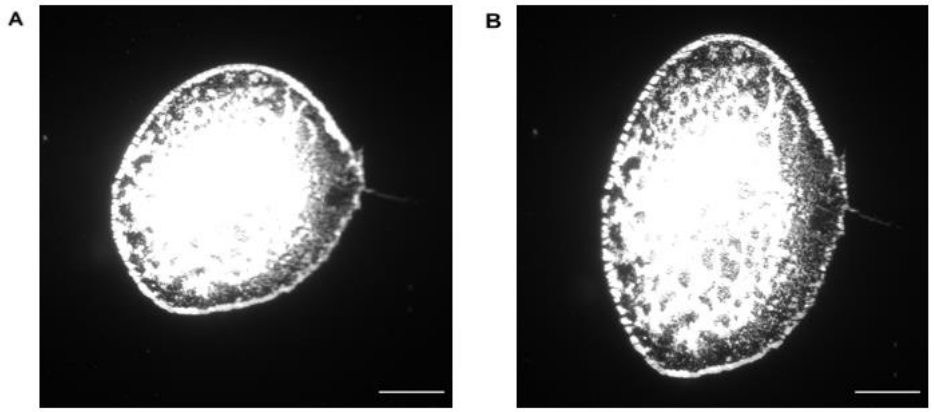

Fig. 3.4: *Fluorescent mark used for membrane strain calibration. (A) Fluorescent mark in relaxed condition (no stretch). (B) Fluorescent mark corresponding to 9 mm displacement of lead screws. Scale bar = 104 µm.*

3.3 Cell stretcher realization: overcoming constraints and achieving objectives

The primary aim of this project was the realization of a cell stretching system which could accurately administer mechanical stimuli to cells in a wide range of strain modes and amplitudes and, simultaneously, observe cell biological response. To accomplish this goal, an accurate definition of the objectives and constraints was crucial for the project design.

Firstly, the necessity of real-time cell monitoring imposed several constraints in terms of microscope compatibility. The ideal device should be mountable on the microscope while retaining the mobility offered by the motorized stage. For this reason, it had to fit dimensional stage limits and it must avoid damages to the microscope components during use. Moreover, the cell stretcher had to be lightweight to not overheat microscope stage motors. The microscope chosen for device validation was the inverted microscope ZEISS Axio Observer Z1. However, adaptability also to other microscopes was required for experimental needs.

To enable real-time cell observation, it was also necessary to implement a symmetric stretching of the membrane. As illustrated in **Fig. 3.5**, this allows us to limit the analysis within a specific field of view during membrane stretching[5], providing more consistent and real-time data for analysis.

As regards the stretching pattern, the desire to explore the cellular response to different types of stretching stimuli imposed several demands to be satisfied. Specifically, the possibility of performing both uniaxial, biaxial and equibiaxial stretching of the cell chamber was required. Moreover, the possibility of deforming the substrate by at least 30% respect to its initial length was necessary. The cell stretcher had to conduct long-term experiments (even overnight) and, for this reason, it was required that the actuators did not overheat excessively. Another important parameter to consider was the cost: in this project, a budget of around 2,000 € was considered for the realization of a low-cost cell stretcher.

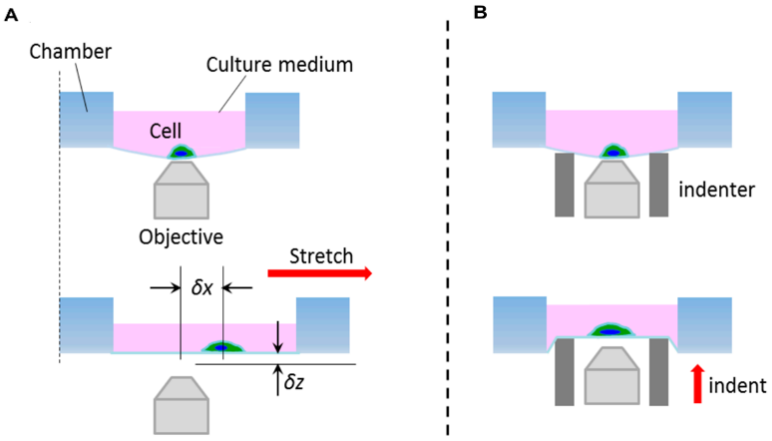

Fig. 3.5: *The importance of symmetry on live cell monitoring. (A) Asymmetrical stretching (from one side) of the cell chamber induces difficulties in the continuous observation of target cells with high magnification objectives because the position of the cells is moved from the field of view. (B) A stretching method for cell imaging applied by Huang et al.[5]. Vertical displacement of the indenter symmetrically stretches the membrane, with target cells that remain in the field of view.*

The project solution is illustrated in the **Fig. 3.6 A**. The device is configured as a cell-stretcher with electromechanical technology as it involves the use of three electric stepper motors. Two of them guide the stretching in one direction, while the third implements the deformation of the stretching chamber in the orthogonal direction with the help of a system of belts and pulleys. Specifically, each motor is coupled with a stainless steel trapezoidal reverse screw which, unlike the usual screw, is composed of a half right-hand and a half left-hand threaded part connected by means of a mechanical joint. In this way, by inserting a pair of lead screws on distinct parts of each screw, there will be a linear translation of them in the same direction but in opposite way, for any rotation direction of the motors. Each lead screw is connected to the opposite one by means of a linear rod, creating a system of orthogonal cross-pieces on which four prismatic-shaped components can slide. Indeed, the latter incorporate within them a pair of linear bearings mounted in orthogonal positions to allow the prisms movement in both directions of stretching. Each prism is connected by means of a bolt to one corner of the cell chamber, enabling the application of both uniaxial and biaxial stretching (with any ratio between the axes). The actuation system consists of Arduino, drivers and stepper motors and implements the control action calculated by the Matlab script. Arduino receives from the latter a string formed by the desired linear advances of the lead screws and, starting from these data, calculates the necessary rotations of the motors to achieve this advancement.

In **Fig. 3.6 B** it is shown the cell stretcher mounted on top of the microscope ZEISS Axio Observer Z1. The integration with the microscope is realized through a plexiglass base which allows the use of the motorized stage. Furthermore, the device can be easily adapted to other microscopes as long as small adjustments are applied to the base. The table **Tab.1** shows, instead, the costs of the individual

components and the total expenditure which was within the pre-established budget.

.

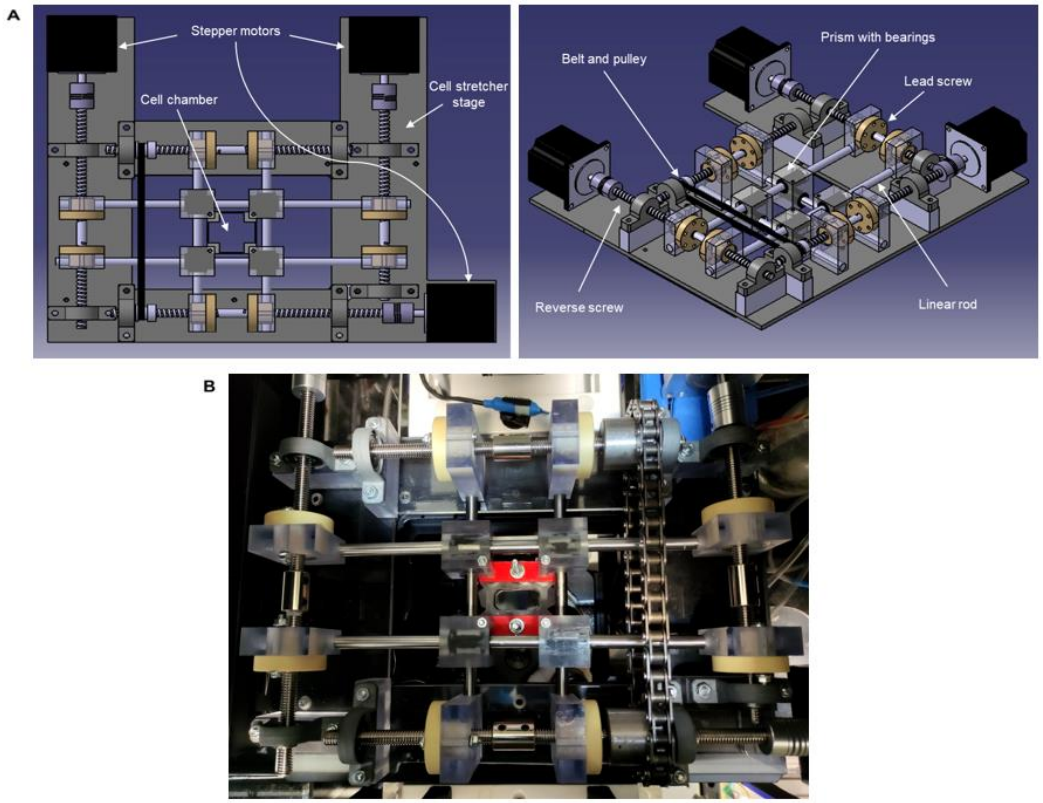

Fig. 3.6: *Cell stretcher design and realization. (A) Illustration of cell stretcher set-up and components in Catia V5 software. (B) Cell stretcher mounted on top of ZEISS Axio Observer Z1 microscope stage.*

Components	Supplier	Number	Unit price (€)
Stainless steel trapezoidal reverse screws 1 m	Igus®	4	204.35
Lead screw dx threaded	Igus®	4	11.45
Lead screw sx threaded	Igus®	4	18.10
Linear rod Φ 8 mm	RS Components	4	13.14
Linear bearing Φ 8 mm	RS Components	8	21.94
Ball bearings with support	Amazon	2	12.99
Mechanical joints	Compass DHM	1	14.99
Belt and pulley	Amazon	1	10.99
Motor holders	Amazon	1	15.99
Stepper motor	RS Components	3	64
Motor driver	Amazon	3	24.28
Elegoo Mega card	Amazon	1	14.99
Power supplies	RS Components	3	141.25
			Total = 1935.21 €

Tab.1: *Table of costs for cell stretcher realization.*

3.4 Cell chamber design and realization

In order to effectively apply stretching stimuli to the cells, the design of a cell chamber was driven by several experimental needs. Firstly, together with the travel distance of the lead screws, the dimensions of the chamber had to be considered for determining the maximum achievable substrate strain amplitude. Moreover, the cell culture region had to be large enough to avoid cell-cell contacts during stretching experiments and, simultaneously, to enable the presence of enough cells for statistical analysis. The interest in investigating cell subcellular components constrained the membrane thickness around 100-200 µm fits with the small working distance of high magnification objectives.

Although the cell stretcher has been designed and realized to potentially perform biaxial stretching, in this research project it was exploited to investigate the cellular response to a purely uniaxial stimulus and the cell chamber geometry design was optimized for this goal.

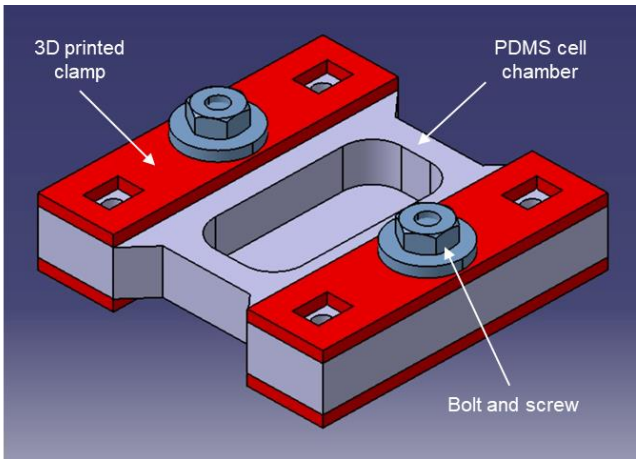

Fig. 3.7: *Custom-made PDMS cell stretching chamber coupled with 3D printed clamps (illustrated in Catia V5 software)*

The final version of the custom-made cell chamber is reported in **Fig. 3.7**. PDMS has been chosen as material due to its biocompatibility, optically transparency and elastic properties. The cell chamber consists of a central bottom, with dimensions of 32 × 15 × 0.1 mm^3, which is uniaxially stretched by two ends. In particular, each of the two walls along the stretching direction is composed of three holes. The two lateral ones are used to mount the chamber on the cell stretcher by connecting them to the prism holes through bolts and screws. The central hole, instead, is used to integrate the wall with 3D printed clamps, enhancing the transmission of strains to the central cell region. Indeed, the coupling of clamps, wall and prisms enables a more uniform distribution of the traction forces in the wall and

avoids the excessive deformation of the holes during stretching.

As previously mentioned in this work, in order to foster a coherent cell biological response to the stretching stimulus, it is essential that cells experience the same strain of the substrate. Therefore, it was necessary to investigate the strain field in the cell culture area of the cell chamber and restrict the cell observation to the uniform strain field region. For this purpose, finite element analysis (FEA) of a solid cell chamber model was performed using Abaqus software. Simulation forces and constraints were defined for a 30% uniaxial strain along the y-axis of the cell culture substrate, which was the maximum desired strain amplitude. Finally, resultant logarithmic strain fields along the x-axis and the y-axis were examined (**Fig. 3.8**). A uniform strain region, reflecting the 31.3% of total culture region area, was found in y direction. Moreover, a 42% uniform area was found in the x direction. Superimposing the axial and transverse strain fields, the overlapping uniform strain area was defined by a central 11 mm width and 7.35 mm height rectangle (16.6% of total culture region area) to which cell observation was restricted.

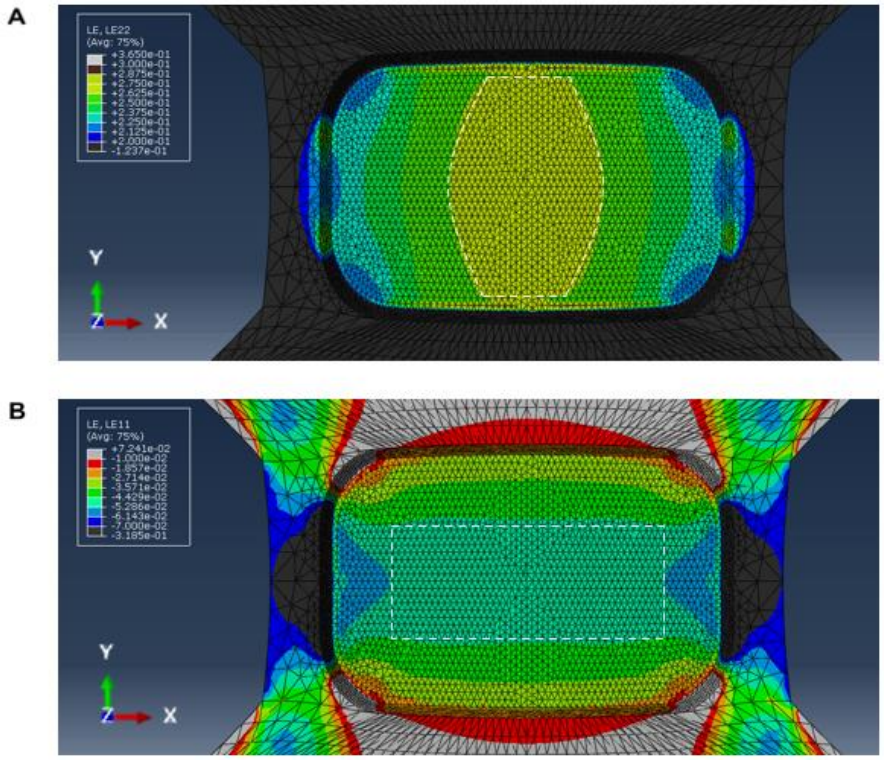

Fig. 3.8: *Finite element analysis (FEA) of the cell stretching chamber subjected to 30% uniaxial strain in y direction. (A) Logarithmic strain field in the longitudinal direction (LEyy) of the cell culture chamber's membrane. (B)) Logarithmic strain field in the orthogonal direction (LExx) of the cell culture chamber's membrane. Uniform strain regions are marked through white dashed lines.*

3.5 Nanopatterned substrate to standardize cell orientation with respect to stretching direction

Although the spatial presentation of the stretching stimulus is uniform in the previously defined cell observation region, the way in which this stimulus is perceived by cells strictly depends on the relative orientation between cells and the applied force. Several studies[6,7] have highlighted how randomly oriented cells solicited by uniaxial substrate stretching, experience varying levels of strain or deformation along different axes. This can lead to disparities in cellular responses, making it challenging to predict how cells will behave under specific mechanical conditions.

In this project, nanogrooved patterned PDMS membrane was implemented in the cell chamber design in order to induce coherent cell alignment along a preferential direction, which will coincide with the direction of the stretching. In particular, the membrane's nanopatterned region consists of a 15 mm^2 square containing parallel and straight channels with a groove and ridge width of 700 nm and depth of 350 nm. The combination with the cell chamber was realized in a way that the nanopatterned region fell within the simulated uniform strain field and the nanopattern direction was parallel to the stretching direction of the cell chamber.

In the **Fig. 3.9**, it is shown NIH3T3 cell polarization in response to the substrate nanometric features after 12 h of culturing. Around 75% of cells displayed an orientation angle within the range [-15°, +15°] with respect to the nanopattern direction (0°). Interesting, also mechanosensing and mechanotransduction subcellular components, e.g., FAs and nuclei, were mostly coaligned with the cell/pattern direction.

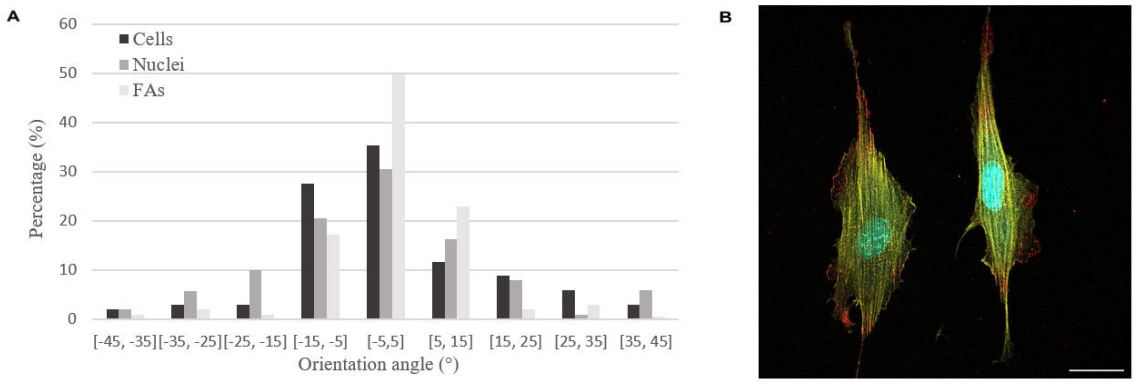

Fig. 3.9: *Orientation analysis of NIH3T3 cells seeded on PDMS nanopatterned substrate. (A) Orientation graph showing cells, nuclei and FAs orientation with respect to the nanopattern direction (0°). (B) Confocal image of focal adhesions (red), actin stress fibers (yellow) and nuclei (cyan) polarized along nanopattern direction. N = 45 cells analyzed, scale bar = 30 μm.*

Current literature has emphasized the fundamental role of nanopattern topographical dimensions in fostering a meaningful cell response in terms of alignment. For example, Loesberg et al.[8] have shown

that the fibroblasts did not possess a noticeable polarization with ridges narrower than 100 nm. Moreover, a groove depth of 100 nm is known as a critical threshold for alignment of several cell types, including fibroblasts[9–11]. In light of this, even if the nanopatterned substrate used in this work showed to be able to induce cell polarization in relaxed condition, the effects of stretching on the morphological features of such nanopattern and their consequential impact on cells mechanosensory capabilities necessitated thorough exploration. For this reason, FE simulations of nanopattern stretching were conducted in Abaqus software. As shown in **Tab.2**, the 30% uniaxial substrate strain only slightly affects the groove/ridge width and the groove depth, which remain in the cell mechanosensing range.

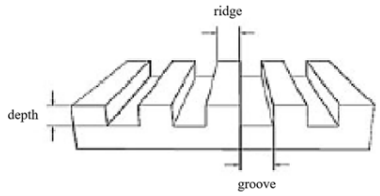

	Relax (nm)	30% uniaxial strain (nm)
Ridge	700	630.1
Groove	700	626.2
Depth	350	313.9

Tab.2: *Deformations of nanogrooved patterned substrate's critical dimensions following 30% uniaxial substrate strain.*

3.6 Optimization of environmental conditions for live cell experiments

After cell stretching device realization, the next step was its integration with the microscope ZEISS Axio Observer Z1 to perform live cell experiments. For this purpose, as previously mentioned, the cell stretcher was designed to perfectly fit the microscope stage and enable real-time cell observation upon stretching. However, beyond the physical integration, the implementation of optimal and stable microscope environmental conditions during experiments represented a noteworthy challenge.

Live cell experiments demand meticulous control over temperature, which must be kept stable at 37 °C. The pH of the culture medium must be maintained at a physiological level (7-7.7 pH), and this requires the cell to be cultured in a 5% of carbon dioxide (CO2) atmosphere. Moreover, environmental 97-100% humidity is necessary to minimize evaporation of the medium, avoiding changes in osmolarity. The maintenance of these environmental parameters at desired and consistent levels is crucial for preserving cell viability and functionality and ensuring the fidelity of experimental outcomes.

ZEISS Axio Observer Z1 microscope is equipped with a large cage incubator in which temperature is stably controlled by recirculating warm air, and a top-stage incubator which fits on the microscope stage and guarantees the desired CO2 and humidity for the cells in a smaller volume. However, the impossibility to use the top-stage incubator due to cell stretcher size and design, imposed the necessity to optimize the environmental condition during live experiments.

A first attempt was made by setting the cage incubator temperature to 37 °C and introducing a synthetic biological buffer, HEPES, in the cell medium to maintain the pH within the physiological range in the absence of a CO2 controlled environment. Culturing cells in these live experimental conditions, nuclear area drastically decreased in just 2 h (**Fig. 3.10**), manifesting the inadequacy of the solution. Indeed, at the end of the experiment, the temperature of the culture medium inside the cell chamber was around 33°C due to the heat loss through evaporation. More than 35% of the medium inside the chamber evaporated after 2 h due to the lack of a humidity control. Furthermore, the medium color turned purple (8 pH) as the use of HEPES in the culture medium only reduced the rate of pH drift and did not eliminate the progressive increase in alkalinity due to the culture exposure to the atmosphere.

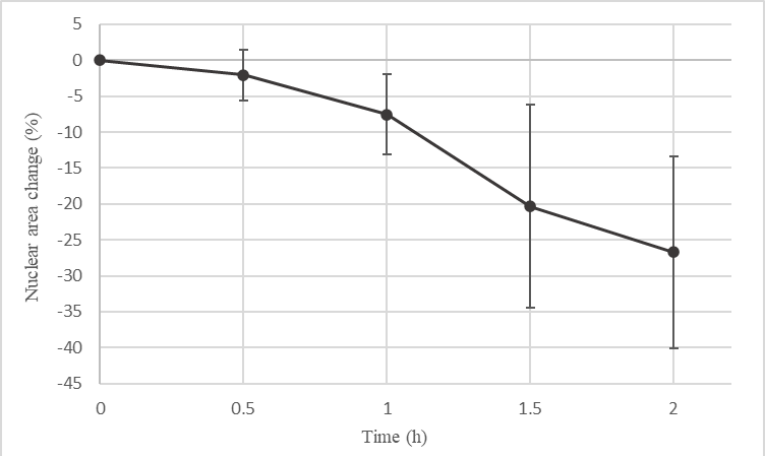

Fig. 3.10: *Nuclear area decreases for cells cultured on the relaxed cell chamber in not-optimized live cell experiment environmental conditions: incubator temperature = 37°, 25 mM HEPES and lack of humidity control. Error bars represent the standard error of the mean. N = 20 nuclei analyzed.*

In order to solve these discrepancies with respect to the cell physiological environmental conditions, some measures have been taken. Firstly, to effectively control the temperature of culture medium, the medium surface in the culture chamber was overlaid with silicone oil. Indeed, the latter is able to effectively decrease medium evaporation and, at the same time, is non-toxic, inert, and highly gas permeable for O2 and CO2. At this point, the cell chamber with culture medium and silicon oil was

placed inside the microscope incubator pre-heated at 37 °C but the medium steady state temperature resulted in around 40 °C. The reasons behind this excessive medium temperature lay in the heating system of the cage incubator. In particular, it employs a temperature unit that generates a hot air jet of 60 °C at the inlet of the enclosure in order to reach and maintain the desired incubator temperature selected by software. In the absence of the top-stage incubator, the cell chamber was continuously hit by the air jet, causing the culture medium overheating. For this reason, the cage incubator temperature was calibrated and a temperature of 34°C was found to induce a steady state medium temperature of 37 °C (**Fig. 3.11 A**).

Regarding the medium pH drift in the presence of HEPES buffer, the main causes were represented by the medium exposure to the atmosphere and the highly gas permeability of PDMS. To solve this issue, the cell stretching chamber was covered with a PDMS cap and, through it, the 5% CO2 air tube was directly connected to the chamber (**Fig. 3.11 B**). The air flux velocity was controlled from microscope software in order to avoid hydrostatic pressure inside the chamber and stabilize the medium pH.

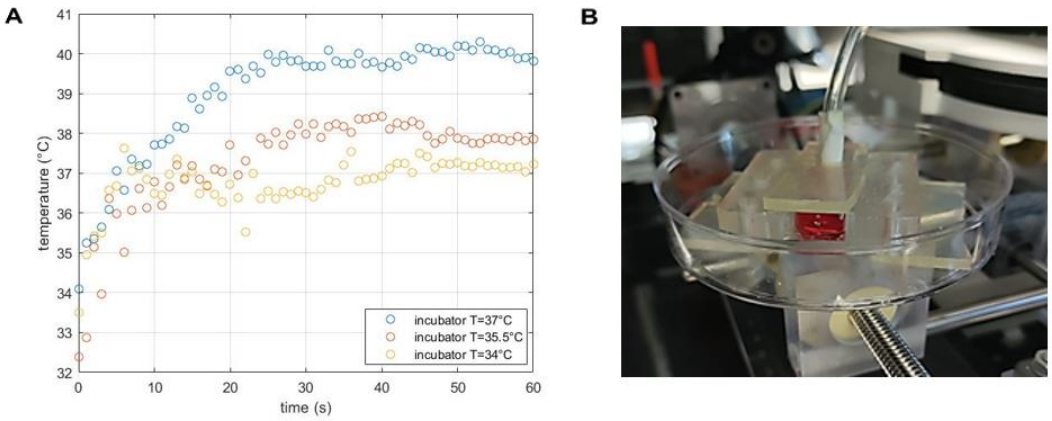

Fig. 3.11: *Optimization of live cell experiment environmental conditions. (A) Calibration of microscope cage incubator's temperature to achieve cell medium's steady state temperature of 37°. (B) Stabilization of medium pH through the insertion of the 5% CO2 air tube directly inside the cell chamber.*

With the described set-up, cell culture medium temperature and pH were successfully maintained in the physiological range for at least 6 h. This can be appreciated also from the **Fig. 3.12**, where it's shown how the nuclear area remains constant over this time period. Optimal environmental conditions were not guaranteed for live experiments longer than 6 h due to the fact that medium evaporation was reduced but not completely eliminated.

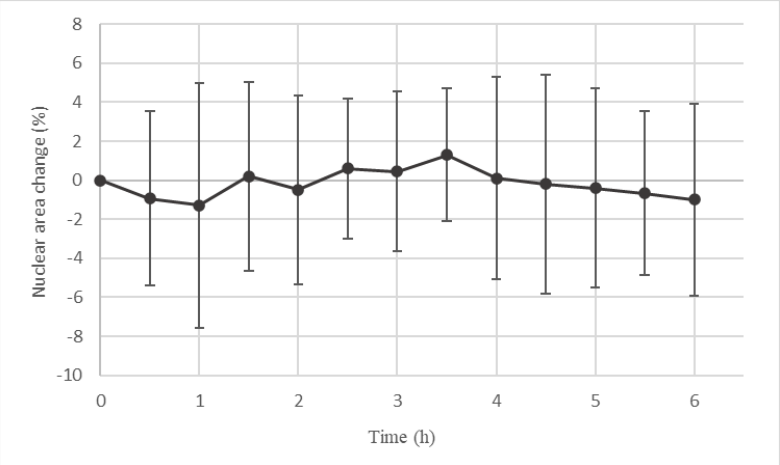

Fig. 3.12: *Nuclear area variations for cells cultured on the relaxed cell chamber in optimized live cell experiment environmental conditions: incubator temperature = 34° and 5% CO2 supply. Error bars represent the standard error of the mean. N = 25 nuclei analyzed.*

3.7 Calibration and validation of cell stretching system

Prior to undertaking stretching experiments involving cells, the meticulous characterization and calibration of the membrane strains emerged as a foundational prerequisite. Indeed, the calibration process is indispensable for ensuring the accuracy and reproducibility of mechanical strain application, as it directly influences the integrity and reliability of subsequent cellular responses.

In order to quantify the relationship between the displacement of lead screws induced by the action of stepper motors and the resultant deformation of cell chamber membrane, fiducial fluorescent marks were placed on the top of membrane surface. In particular, marks of irregular shapes in the uniform strain region were obtained through the evaporation of small solution drops containing green fluorescent beads. Incremental cell stretcher lead screws displacements of 1 mm were applied by software and the longitudinal and transverse strains of fiducial marks were calculated to evaluate the local strains of cell chamber membrane. Strain results were used to construct a calibration curve (**Fig. 3.13**), in which a relatively linear relationship between lead screws movement and y-axis deformation can be appreciated. In particular, the cell stretching device can apply precise uniaxial stretching stimuli up to 30% amplitude, corresponding to a 9 mm lead screw displacement. Displacements above this value led to sudden cases of breakdown of the cell stretching chamber.

Exploiting the fluorescent marks distributed at different locations of the chamber membrane, the strain along both the longitudinal and transverse directions was verified to be uniform (within the 5% error respect the average strain value) throughout the strain region previously extracted from FE

simulations. It is also important to note that, in correspondence of the 30% uniaxial strain in the y direction, the calibration result for the membrane strain in the x direction (around – 4.3%) deviates from the simulated value with a discrepancy of 22.8%. This could be due to the addition of PBS to the cell culture chamber to replicate the weight force of the cell culture medium on the PDMS membrane during the calibration process. Indeed, the latter was not taken into account in the simulations.

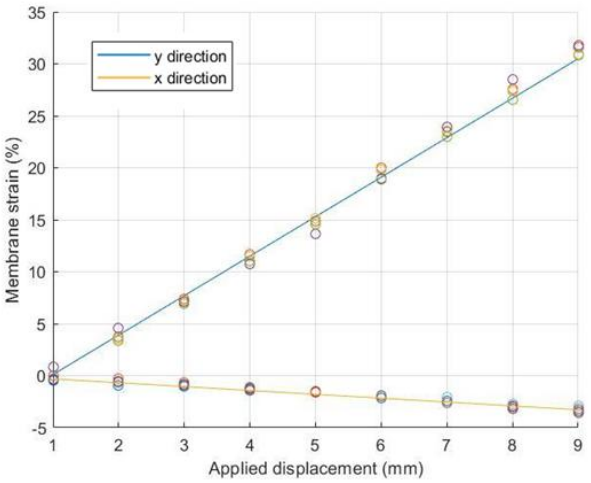

Fig. 3.13: *Calibration of cell chamber substrate strains.*

3.8 Discussion

The motivation behind this work stems from the necessity to develop advanced tools for understanding and finely controlling cell mechanobiological response to mechanical doses. While commercially available stretching devices offer certain advantages, their limitations in terms of costs, customization, and functionality led to the realization of a highly flexible, low-cost cell stretching system capable of providing controlled mechanical doses to cells.

The developed system is driven by an electromechanical setup and allows the application of precise uniaxial strains (up to 30%) to the PDMS cell chamber membrane. However, the biaxial mode and higher strain amplitudes could be easily achieved by optimizing cell chamber design and dimensions. The challenging integration of the device with the microscope's stage and incubator was crucial to enable the real-time cell observation and ensure the stability of environmental parameters for up to 6 hours of continuous live cell experiments. This time limitation is due to the lack of incubator's humidity control that causes an excessive evaporation of cell culture medium through the PDMS cell

chamber. One solution could be to direct a jet of humidified air directly onto the stretching chamber, extending the duration of live experiments.

As previously mentioned, the main goal in the design of this stretching system was the administration of “univocal” mechanical stimuli to a cell population, enhancing the control over cellular response. This was achieved through the introduction of topographical cues which demonstrated to successfully polarize cells in the stretching direction and, therefore, standardize the cells perception of stretching stimuli. Moreover, the spatial uniformity of these signals was guaranteed in the observation region through the FEA of the stretching chamber.

In this way, the device described in this chapter stands as a powerful and versatile tool which could provide a valuable help in understanding and manipulating cellular responses to mechanical stimuli, significantly advancing our knowledge in cell mechanobiology and mechanomedicine field.

3.9 References

1. Hinkle, E. R. et al. Stretching muscle cells induces transcriptional and splicing transitions and changes in SR proteins. Commun. Biol. 5, 987 (2022).

2. Shyu, K.-G. Cellular and molecular effects of mechanical stretch on vascular cells and cardiac myocytes. Clin. Sci. 116, 377–389 (2009).

3. Xu, J., Wang, Q., Li, X., Zheng, Y. & Ji, B. Cellular mechanisms of wound closure under cyclic stretching. Biophys. J. 122, 2404–2420 (2023).

4. Maruoka, M. et al. Abi-1-bridged tyrosine phosphorylation of VASP by Abelson kinase impairs association of VASP to focal adhesions and regulates leukaemic cell adhesion. Biochem. J. 441, 889–901 (2012).

5. Huang, W., Zhang, S., Ahmad, B. & Kawahara, T. Three-Motorized-Stage Cyclic Stretching System for Cell Monitoring Based on Chamber Local Displacement Waveforms. Appl. Sci. 9, 1560 (2019).

6. Tsukamoto, S. et al. Compressive forces driven by lateral actin fibers are a key to the nuclear deformation under uniaxial cell-substrate stretching. Biochem. Biophys. Res. Commun. 597, 37–43 (2022).

7. Chen, Y., Pasapera, A. M., Koretsky, A. P. & Waterman, C. M. Orientation-specific responses to sustained uniaxial stretching in focal adhesion growth and turnover. Proc. Natl. Acad. Sci. 110, (2013).

8. Loesberg, W. et al. The threshold at which substrate nanogroove dimensions may influence fibroblast alignment and adhesion. Biomaterials 28, 3944–3951 (2007).

9. Wang, P.-Y., Yu, J., Lin, J.-H. & Tsai, W.-B. Modulation of alignment, elongation and contraction of cardiomyocytes through a combination of nanotopography and rigidity of substrates. Acta Biomater. 7, 3285–3293 (2011).

10. Tsai, W.-B., Ting, Y.-C., Yang, J.-Y., Lai, J.-Y. & Liu, H.-L. Fibronectin modulates the morphology of osteoblast-like cells (MG-63) on nano-grooved substrates. J. Mater. Sci. Mater. Med. 20, 1367–1378 (2009).

11. Tsai, W.-B. & Lin, J.-H. Modulation of morphology and functions of human hepatoblastoma cells by nano-grooved substrata. Acta Biomater. 5, 1442–1454 (2009).

Chapter 4

Calibration of uniaxial stretching stimuli delivered to the cells

4.1. Introduction

How cell behavior is influenced by mechanical stimuli continues to be an open question. We can certainly try to answer this query focusing the attention on the way by which cells integrate and convert biophysical cues into intracellular biochemical signals, in a process that involves multiple mechanosensing and mechanotransduction subcellular components[1].

Focal adhesions (FAs) act as the first mechanosensors that transmit mechanical forces between the cytoskeletal contractile machinery and the ECM. Indeed, FAs are composed of a subset of scaffolding and regulatory proteins, referred to as force-sensitive or force-responsive proteins, which connect the actin cytoskeleton to integrin receptors. The propagation of extracellular and cell-generated forces is ensured by the regulation of cytoskeleton tension[2]. Mechanical force could promote the level of cellular tension in a positive feedback loop through the association of specific FA components that allows the maturation of FAs and reinforces the cytoskeleton stress fibers (SFs)[3]. In particular, the relocation of FA protein zyxin and other crosslinkers upon mechanical loading fosters SFs reinforcement and increases cytoskeletal tension[4]. On the other hand, SFs contractility prompts talin unfolding and vinculin recruitment to the FAs[5], where the proteins participate in FA composition and organization[6,7].

The mechanical information arising from modifications of the ECM, perceived by the FAs and propagated at the cytoskeleton level, eventually direct nuclear mechanotransduction. The nuclear-cytoskeletal coupling is crucial for force transmission to the nucleus and, consequently, for the mechanical regulation of nuclear epigenetics and cell functions[8,9].

In this strictly interconnected system, it seems clear that the way by which the individual cell's mechanosensory components perceive and respond to the external forces plays a crucial role in determining the collective cell biological response. For this reason, in the realm of effectively calibrating the mechanical stimulation to induce specific cellular functions, it becomes prelusive to

understand the mechanosensing and mechanotransduction pathway of the "mechanical dose" applied to the cells.

To this aim, in this study we investigated cell response to sustained uniaxial substrate strain, focusing the attention on the propagation of the stretching stimulus from the adhesion sites towards the cell nucleus. In particular, mouse embryo fibroblasts (NIH3T3 cell line), aligned in the direction of stretching on nanogrooved elastic membrane, were subjected to two different substrate strain levels, i.e., 8% and 29%. The first stain magnitude of 8% was selected considering the literature supported existence of a lower threshold of 3% regarding the ability of cells to sense and respond to mechanical deformation[10], and the strain levels range [5-15%] to which most tissues are subjected in physiological conditions[11–13]. Conversely, the 29% strain level was chosen to account for also the large deformations (> 20%) experienced by certain tissue, like the solid tissues of hollow organs (e.g., bladder) and skin[14,15]. Moreover, although significant pathology can arise if relatively large stretches are sustained[16,17], the responses of cells are not known at these levels of sustained strain.

Morphological and fluorescence intensity variations of subcellular components were evaluated after membrane stretching experiments at different time points by means of live fluorescence imaging. More specifically, the analysis was performed: 1) before the stretching of the substrate to evaluate cell's basal state, 2) immediately (2 min) after to capture the cellular elastic response to the deformation, 3) 15 min after the stimulation to evaluate the transient effects of cell stretching in a timeframe compatible with the times of assembly-disassembly of FAs[18,19], and 4) 2 h after stretching to assess cell response when the processes of mechanotransduction associated with the mechanical stimulus and involving the cell's cytoskeleton and nucleus can be considered partially/totally actuated (**Fig. 3.14**).

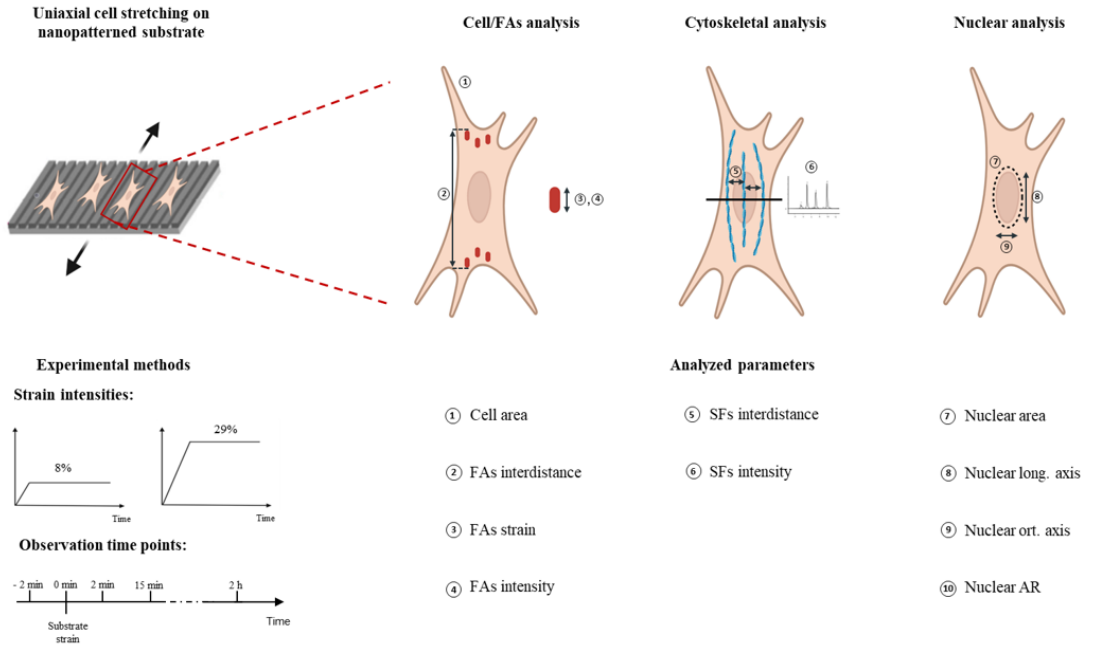

Fig. 4.1: *Graphical representation of experimental methods and analysis.*

4.2. Materials and methods

4.2.1. Cell culture

Mouse embryo fibroblasts NIH3T3 cell line has been cultured at 37°C in 5% CO2 in humidified incubator in Dulbecco's modified Eagle's (DMEM) high glucose medium (Sigma-Aldrich, D5671) supplemented with 10% bovine calf serum (Sigma-Aldrich, C8056), 1% L-glutamine (Sigma, St. Louis, MO), and 1% sodium pyruvate (ThermoFisher). Prior to cells seeding, cell stretching chamber was sterilized by ultraviolet exposure for 1 h and, then, chamber culture surface was incubated with 50 ug/ml of human fibronectin for 1 h at 37 °C. At the end of coating procedure, cells were seeded at a density of $1 \cdot 10^3$ cells/cm^2 and left to spread for 24 h in the incubator. The day after, for live experiments, the cell medium was supplemented with 25 mM HEPES (ThermoFisher), and the cell chamber was mounted on the cell stretcher device.

4.2.2. Live cell imaging

Live cell fluorescence imaging experiments were performed on ZEISS Axio Observer Z1. After 24 h from seeding inside the cell chamber, cell culture medium was replaced with 2 ml of 25 mM HEPES (ThermoFisher), and the chamber was mounted on the cell stretcher device inside the pre-heated microscope incubator. To maintain the medium pH in the physiological range, the cell stretching chamber was covered with a PDMS cap and, through it, the 5% CO2 air tube was directly connected to the chamber. Subsequently, sustained uniaxial strains of 8% or 29% were then applied to the cell culture elastic membrane by distancing the lead screws of 3 mm or 8.5 mm respectively. Control experiments were instead conducted in relaxed (0% strain) conditions. Cell images were acquired before, immediately (2 min) and 15 min after the application of the stretching stimulus. In particular, the 2 min time point takes in consideration the time necessary to follow cells during stretching and the time of acquisition of the image. Transmission and fluorescence images were collected with the 63x oil immersion objective and preliminary experiments were carried out to optimize image settings in order to minimize phototoxicity and photobleaching.

Live cell fluorescence imaging experiments for cytoskeletal analysis were conducted on ZEISS LSM 700 confocal microscopy. Even this time, environmental conditions inside the microscope incubator were optimized to allow live experiments and images were collected with 63x oil immersion objective.

In all the experiments, only the cells highly polarized in the range [-15°, 15°] along the nanopattern direction (0°) were considered for the analyses.

All the parameters (P) analyzed in this thesis were expressed as percentage variation respect the initial condition (before stretching) and they were computed at different time points and for all strain levels in the following way: $\%Pi = ((Pi - Po) / Po) \cdot 100$, where Po is the cellular parameter measured before stretching, while Pi is the parameter of the same cell measured at time i. Then the mean of the percentage variations was presented in the graphs for each time point and strain level. All the analyses were performed in software Fiji.

4.2.3. Cell transfection and nuclear staining

NIH3T3 cells were seeded in a 35mm petri dish at 80% confluency and left overnight in the incubator at 37°C and 5% CO2. Cells were then transiently transfected with paxillin-RFP, talin-GFP or Lifeact-GFP depending on the type of experiment to perform. The transfection complex

was prepared in Opti-MEM reduced serum medium (GIBCO) and Lipofectamine 3000 (ThermoFisher) was used as a transfection reagent. The amount of DNA/LIPO3000 was determined following the supplier's instruction. Briefly, after 6 h of incubation with 1.75 μg (paxillin-red), 2.5 μg (talin-GFP) or 1.25 μg (Lifeact-GFP) of pDNA in lipoplexes, incubation medium was replaced with complete cell culture medium. After 24 h in the incubator, cells were seeded on a cell stretching chamber and the live experiments were conducted after another 24 h.

For cytoskeletal and nuclear analyses, nuclei of cells seeded on the cell chamber were stained with Hoechst 33342 (1:10,000 in culture medium) for 20 min. Then, the incubation medium was replaced with 2 ml of complete cell culture medium.

4.2.4. Cell area and FAs interdistance analysis

Cell spreading area was extracted from live cell transmission and fluorescent (Lifeact-GFP) images. In particular, cells were manually contoured in transmission images and thresholded in fluorescent images. Cell area was measured with the measure command. Cell area percentage variations on the same cells were computed with respect to the cell area calculated at initial condition at different time points and for all strain levels. The expected substrate area changes were computed for each strain level considering the longitudinal and orthogonal strains extracted from the membrane calibration in the previous chapter.

FAs analysis was conducted on fluorescent images of paxillin-red and talin-GFP transfected cells. To compute the FAs spatial displacement on the substrate in response to stretching, the interdistance between FAs in the direction of stretching (which coincides with the direction of cell polarization on nanopattern) was measured manually by tracking a line parallel to the strain direction between two FAs chosen in the opposite positions respect to the cell centroid. In particular, the end points of this line coincided with the two FAs outer pixels with respect to the cell centroid in the direction of the line. The contrast of each fluorescence image was enhanced before the analysis. Moreover, around 5 interdistances were randomly selected from each image from a total of 30 cells. The percentage variations of parameters in this section were computed as shown in the section 4.2.2.

4.2.5. FAs analysis

FAs analysis (length and intensity percentage variations) was conducted on fluorescent images of paxillin-RFP and talin-GFP transfected cells. Digital images of FAs were firstly processed using the blur command. Blurred images were then subtracted from the original images using the image calculator command. The images were further processed with threshold command to obtain binarized images.

For the length analysis, the contours of single FAs were selected with the wand tool from the digital cell images before stretching and the contours of the same FAs were selected in the subsequent time points after stretching. The FAs length value in the direction of stretching was extracted from the contours' height parameter in Fiji. To avoid measurement errors and obtain length variation above the image resolution, only the FAs characterized by an initial (before stretching) length (Lo) > 4 μm for control and 8% strain conditions, and Lo > 1 μm for the 29% strain condition were considered in this analysis.

The FAs mean intensity was instead measured by transferring the FAs contours (selected on digital images) on the original fluorescent images. The mean background intensity of each image was calculated by averaging the means of different ROI selected outside the fluorescent cell signal. The mean intensity of each FA was then calculated by subtracting the background mean intensity of the image to the FA mean. For the analysis of "coherent" and "incoherent" paxillin marked FAs, a FA was considered "coherent" to the substate if its length percentage variation immediately after stretching was lower than the 10% for the 8% substrate strain level, and lower than the 31 % in the case of 29% substrate strain. Otherwise, it was considered "incoherent".

The percentage variations of these parameters were computed as shown in the section 4.2.2. Around 10 FAs per cell were analyzed for a total of 28 cells.

4.2.6. Cytoskeletal SFs analysis

Cytoskeletal analysis was conducted on confocal fluorescent images of Lifeact-GFP transfected cells, whose nuclei were stained with Hoechst 33342. For this analysis, only the SFs covering the nuclei were considered from Lifeact z-stack images by z-projecting (sum intensity) only the slides containing their fluorescent signal. On the resultant images, a line

perpendicular to the stretching direction (which coincides with the SFs polarization direction) was drawn above the nuclei and, along this line, the pixel intensity of SFs as function of the distance was plotted in Fiji with the command “plot profile”.

The interdistances between the highest peaks in the graph were measured considering the spatial distance between the highest point of a peak and the one of the consecutive peak along the drown line, and so on. Then, the mean of the interdistances was calculated for each image and for the different experimental conditions.

The SF intensity, instead, was referred to as the pixel intensity corresponding to the highest point of the peak. In this way, the mean SFs intensity for each image was evaluated by averaging the peaks maximum intensities.

The percentage variations of SFs interdistance and intensity were calculated as seen in the section 4.2.2.

4.2.7. Nuclear morphological analysis

The morphological parameters (axes length, aspect ratio (AR) and nuclear area) were extracted from images of live cells stained with Hoechst 33342. Nuclear images were converted to binarized masks using appropriate threshold selected manually in Fiji. Then, nuclear outlines were selected using the wand tool and the useful parameter extracted from the measure command. In particular, the nuclear longitudinal and orthogonal axes with respect to the stretching direction were referred to as the major and minor parameters, respectively, in Fiji. The AR was then computed as the ratio between major and minor. Again, percentage variations of morphological parameters were calculated as shown in section 4.2.2.

4.2.8. Drug treatment

ML-7 (SigmaAldrich) was used as a selective inhibitor of myosin light chain kinase to decrease cell cytoskeleton contractility. Cells seeded on the cell chamber were stained with Hoechst 33342 and treated with ML-7 (25 μM) 1 h before live cell stretching experiments. Afterwards, the cell chamber was mounted on the cell stretching device to evaluate the nuclear deformability in response to stretching. Nuclear longitudinal and orthogonal axes variations

were calculated immediately (2 min) after the 16% uniaxial substrate stretching. Under the same strain level, a control experiment was conducted on nuclei of untreated cells. Around 5 cells per condition were evaluated. To evaluate the cell response at 2 h from the application of the sustained stretching stimulus, live cell experiments were conducted on ZEISS Axio Observer Z1 microscope.

4.2.9. Long-term experiments

For cell spreading area and longitudinal axis analyses, transmission images of the same cells were acquired before and after 2 h from stretching. Moreover, in a different experiment, fluorescent images of the same cells transfected with paxillin-red, whose nuclei were stained with Hoechst 33342, were acquired in the same way. Control experiments were also conducted on unstretched chambers.

Cell and nuclear morphological parameters were calculated as explained in the previous sections. Cell longitudinal axes instead were extracted from the height of the cells' contours. FAs images were firstly binarized as illustrated in the previous sections and, then, particle analysis was performed in order to determine the morphometric descriptors. FAs length in the direction of stretching was referred to as the height parameter extracted in Fiji. Subsequently, the mean of all the FAs lengths was computed for each image and for all the experimental conditions. Only FAs whose area was above 1 μm^2 were included in the analysis.

Eventually, the percentage variations at 2 h of the calculated parameters were calculated with respect to the initial condition (before stretching).

4.3. Substrate strain propagation to cells through FAs

Several works have widely demonstrated the ability of mechanical stretching to regulate cell morphology[23], orientation[24], cytoskeleton structure[25] and gene expression[26]. Nevertheless, the way by which the stretching stimulus is perceived and integrated by the cell has not been fully unraveled yet. During cell stretching experiments, the substrate deformation is directly transferred to the cell through the focal adhesion contacts, which anchor the cell to the substrate and mediate their communication. Therefore, the quantitative relationship between substrate stretching and FAs spatial reorganization

is crucial to evaluate the amount of mechanical stimulus actually perceived by the cells.

To this aim, the interdistance between FAs in the direction of stretching and the spreading area of NIH3T3 fibroblasts were evaluated in response to sustained uniaxial substrate stretching and compared to the expected values estimated from the calibration substrate strains. This analysis was conducted at two different time points, 2 min and 15 min after stretching, where cells transfected to express a fluorescent talin and paxillin protein were subjected to two different strain levels, 8% and 29%. Moreover, cells cultured in an unstretched chamber (0% substrate strain) were analyzed and used as a control.

As it is shown in the **Fig. 4.2 A**, immediately after stretching the percentage variation of FAs interdistance coincided with the substrate strain level, indicating that the FAs translated according to the substrate. Only for 29% strain, a small decrease of the interdistances was detected after 15 min.

The average cell spreading area for each experimental condition was plotted in **Fig. 4.2 B**, together with the estimated substrate area change (dotted line). The average cell spreading area increased in response to the uniaxial strain. However, even if the substrate deformation is efficiently transmitted to cells in terms of FAs interdistance variation, it was found a discrepancy with respect to the expected substrate area changes (7.1% and 25.1% for the strain levels of 8% and 29%, respectively). This could be explained considering that cells are strongly attached to the substrate only through the mature adhesion sites, while cell membrane-substrate weak interactions and early-stage FAs may not possess the sufficient adhesion force to affinely follow the substrate deformation. After 15 min, cell area did not change under 8% sustained stain, while decreased significantly ($p < 0.01$, Appendix Tab. B) for the higher strain level.

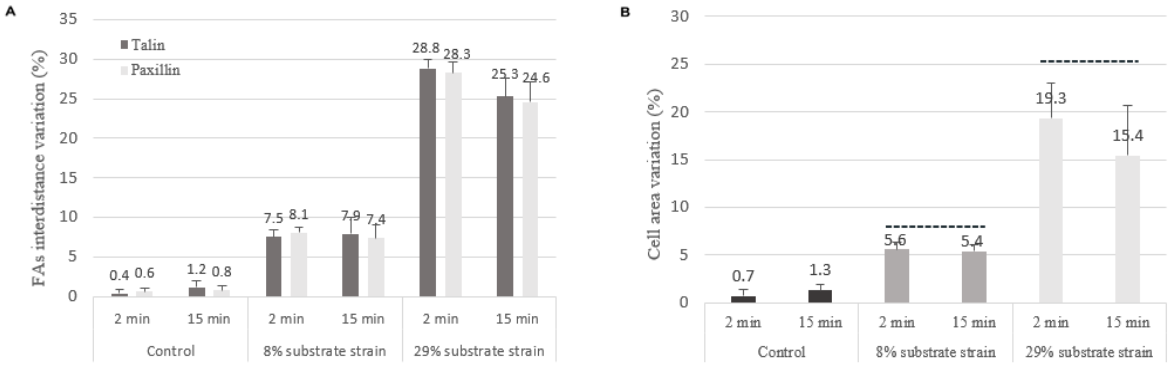

***Fig. 4.2**: Quantitative relationship between substrate and cell stretching. A) FAs, marked through talin and paxillin, interdistance percentage variations respect to the initial condition as function of time and substrate strain. For statistical analysis see Appendix Tab. A. B) Cell area percentage changes with respect to the initial condition as function of time and substrate strain. The dotted lines correspond to expected substrate area changes estimated from the calibration. For statistical analysis see Appendix Tab. A. Error bars represent the standard error of the mean. A total of N = 150 interdistances, extracted from 10 cells per each condition (control, 8% and 29% strain), were analyzed over time for FAs interdistance analysis. While N = 10 cells per each condition were analyzed for the cell area variation analysis.*

By combining live fluorescence imaging and uniaxial stretching, our data showed that substrate strain and FAs displacement is a precise parameter that assesses the effective transmission of the stretching stimulus to the cell. Moreover, analyzing the transient cell response after 15 min, we observed a slight retraction of cell area under the 29% sustained substrate strain, suggesting a global mechano-adaptation process to the elevated substrate deformations.

4.4. FAs dynamic response to substrate strain

Physical forces can modulate the dynamics and interaction of the different FA proteins, altering their composition and organization that in turn influence cellular functions[27,28].

In this study, the effect of substrate stretching on FAs organization was investigated by following the dynamics of two adhesion proteins: talin and paxillin.. Talin can be referred to as a mechanosensitive molecule, which actively senses and responds to mechanical forces by undergoing conformational changes. Signaling proteins, like paxillin, are instead involved in transmitting the mechanical signal inside the cell, initiating downstream signaling cascades.

The dynamic adaptation of FAs was evaluated through the measurement of the FAs length and intensity changes generated by stretching cells expressing fluorescently tagged talin and paxillin by means of cell transfection. Then, the rapid (2 min) and delayed (15 min) FAs response was assessed for 8% and 29% substrate strain intensities.

Fig. 4.3 A shows representative time sequences of NIH3T3 cells with FAs oriented in the stretching direction through on the nanogrooved membrane and subjected to uniaxial strain. The analysis on FAs length variation as function of time and strain level is reported in **Fig. 4.3 B**. Immediately after stretching, the length of both talin- and paxillin-FAs significantly increased (Appendix Tab. C) with respect to the control condition, indicating the effective transmission of substrate strain to the cell adhesion contacts. However, the two mechanoresponsive proteins displayed a different behavior. Talin-FAs strains (7.2 % ± 3.2 % and 30.4 % ± 2.3 %) were conformed with the ones applied to the substrate (8% and 29%), while, in the case of paxillin-FAs, the percentage length increments were significantly higher (14.2 % ± 20.1 and 77.6 % ± 110.3 %). These differences vanished after 15 min from stretching as the paxillin-FAs strains decreased and matched the talin-FAs ones.

Another important difference in the dynamic response of the two proteins composing FAs was found by plotting the relative changes of FAs mean fluorescence intensity (**Fig. 4.3 C**). Talin mean intensity decreases as a function of substrate strain and remains constant over time. This intensity reduction

could be attributed to the spatial spreading of fluorescence signals on larger FAs areas. Conversely, paxillin mean raised as a function of strain and, after 15 min, decreased to values still significantly higher (Appendix Tab. D) than the control condition. These results suggest the paxillin recruitment at the analyzed sites and that, according to the decrease of paxillin-FAs length, it is not stable in time.

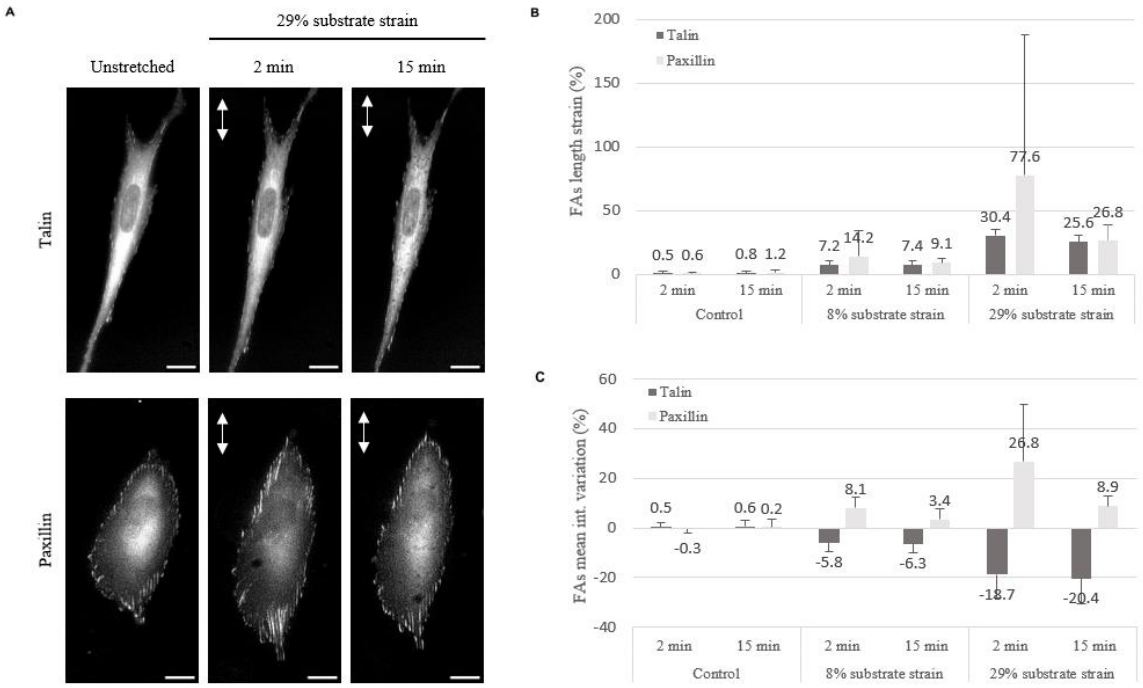

Fig. 4.3*: FAs response to sustained uniaxial substrate strain. A) Fluorescent images of talin and paxillin marked FAs subjected to 29% substrate strain. The white arrows indicate the stretching direction (scale bar 20 µm). B) FAs length percentage changes respect to the initial condition as function of time and substrate strain. For statistical analysis see Appendix Tab. C. C) FAs mean intensity percentage changes with respect to the initial condition as function of time and substrate strain. For statistical analysis see Appendix Tab. D. Error bars represent the standard error of the mean. N = 240 FAs for strain conditions (8% and 29% strain) and N = 40 FAs for the control were analyzed over time, for a total of 28 cells*

To explain the different behavior of talin and paxillin in terms of FAs length strain immediately after stretching, further analyzes were conducted on paxillin marked FAs. A closer look revealed that the length increment beyond the mere increase due to the mechanical stretching of the substrate, can be attributed exclusively to certain FAs (**Fig. 4.4 A**). In particular, the paxillin-FAs population can be divided in two categories based on their immediate response to substrate strain: the "coherent" FAs, which represent the greater portion (**Fig. 4.4 B**) and whose length increment was consistent with substrate strain, and the "incoherent" FAs, referred to those that exhibited a divergence in the strain response compared to the substrate. As shown in Fig. **4.4 C, E**, the length strain of "incoherent" FAs dramatically increased as a function of substrate strain level, followed by an increase of paxillin intensity. However, over a period of 15 min, we observed a partial dissipation of the paxillin recruited at these sites whose morphological and intensity parameters dropped to values comparable with the

"coherent" FAs.

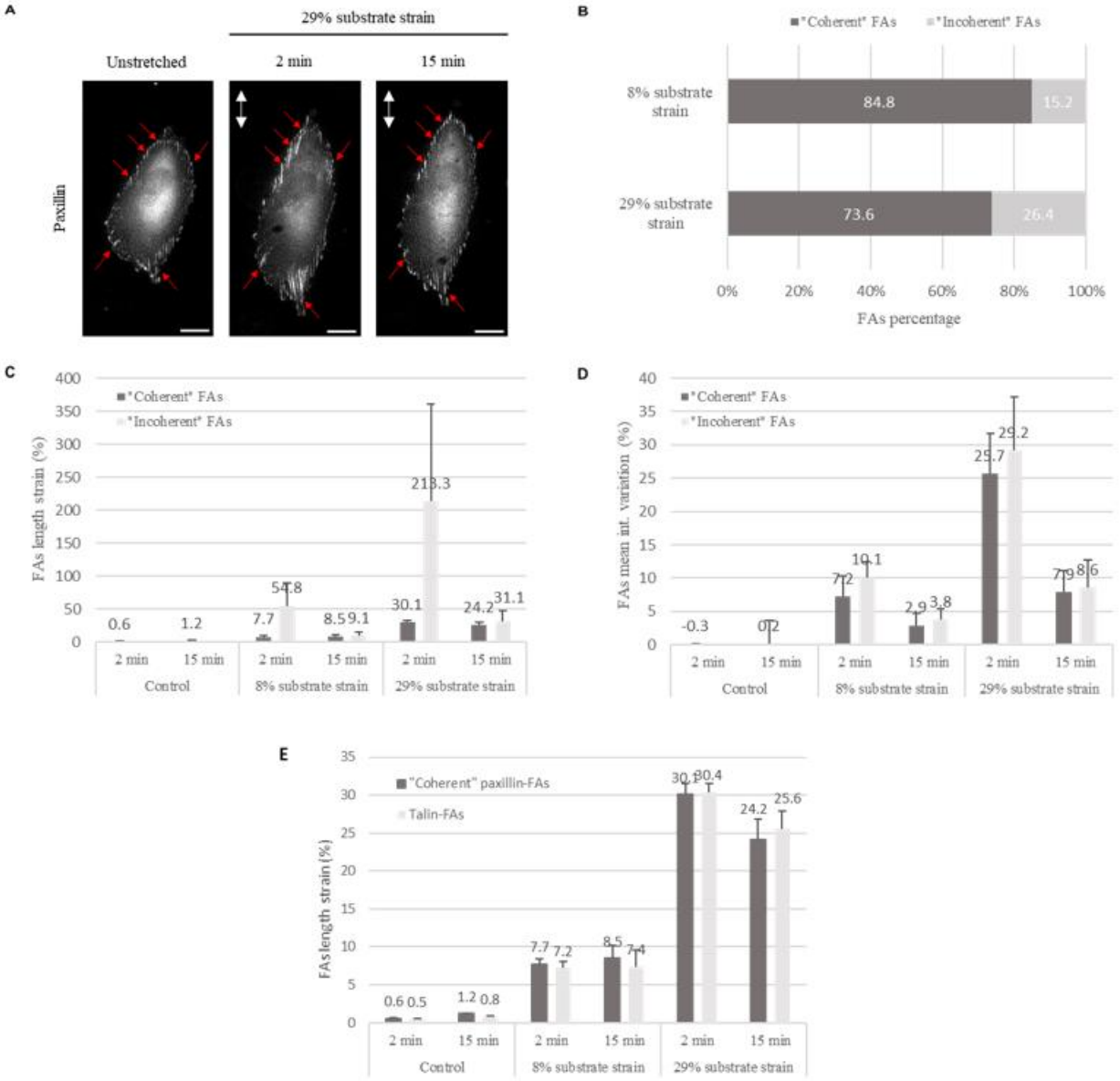

***Fig. 4.4**: Paxillin-FAs categorization in "coherent" and "incoherent" FAs in response to sustained uniaxial substrate strain. A) Fluorescent images of paxillin tagged FAs subjected to 29% substrate strain, showing "incoherent" FAs (indicated by red arrows). The white arrows indicate the stretching direction (scale bar = 20 μm). B) FAs percentage number of "coherent" and "incoherent" FAs as function of substrate strain. C) "Coherent" and "incoherent" FAs length changes with respect to the initial condition as function of time and substrate strain. For statistical analysis see Appendix Tab. E. D) "Coherent" and "incoherent" FAs mean intensity changes with respect to the initial condition as function of time and substrate strain. For statistical analysis see Appendix Tab. F. E) Comparison between "coherent" paxillin-FAs and talin-FAs length changes with respect to the initial condition as function of time and substrate strain. For statistical analysis see Appendix Tab. G. Error bars represent the standard error of the mean. N = 120 FAs for the strain conditions (8% and 29% strain) and N = 20 FAs for the control were analyzed over time, for a total of 14 cells.*

Recent studies have suggested that paxillin, generally described as a FA component, is also found in the cell cytoplasm where it is involved in a mechanoresponsive mechanism that maintains the cytoskeleton SFs homeostasis[29,30]. In particular, in response to mechanical strain, paxillin appears to be rapidly recruited to actin SFs to mediate the repair and stabilization of these sites. Sawada e

Sheetz[31] reported the stretch-dependent binding of paxillin to Triton X-100 cytoskeletons of L-292 cells by two-dimensional gel electrophoresis. Triton X-100–insoluble cytoskeletons were stretched by 10% on collagen-coated silicone and incubated with biotinylated cytoplasmic proteins. Another observation was made from Smith et al.[32], who detected the accumulation of paxillin to SF strain sites on transiently transfected paxillin-mApple and Lifeact-GFP mouse fibroblasts.

We assume that our results further confirm these findings. By quantitative analysis of paxillin-FAs under stretching, we demonstrated that paxillin is recruited at maximum stress sites of SFs, in proximity of FAs, and provided a spatial characterization of this phenomenon as a function of substrate strain. Moreover, we observed that this recruitment was completely extinguished within a time period lower than 15 min.

The dynamic adaptation of FAs under sustained uniaxial strain can be therefore derived from the length strains of "coherent" paxillin-FAs and talin-FAs (**Fig. 4.4 E**). Indeed, no statistical differences (Appendix Tab. G) were observed between the latter. The results indicate the efficient transmission of substrate strains to FAs immediately after stretching. Furthermore, while FAs strains remain constant over time in the case of 8% substrate strain, they significantly decrease after 15 min under 29% strain level indicating a destabilization of FAs induced by the high substrate strain.

4.5. Substrate strain propagation to the nucleus through cytoskeleton SFs

The nucleus is mechanically connected to the surrounding extracellular environment via the cytoskeleton networks. Actin cytoskeletal forces from SFs have been suggested to ultimately propagate the mechanical stimuli to the nucleus in terms of forces and deformations. In turn, the latter could physically stretch or compress chromatin, alter DNA packing, and affect gene regulation[33–35]. Therefore, understanding the cytoskeleton response under mechanical perturbation is crucial to clarify the mechanosensing mechanism of the nucleus.

To define the relationship between substrate strain and the subsequent intracellular distribution of cytoskeleton generated forces, quantitative analyses were conducted on live confocal images of NIH3T3 cells transfected with Lifeact and stained for nucleus with Hoechst 33342. In particular, a line perpendicular to the stretching direction was drawn above the nuclei and, along this line, the pixel intensity of SFs was plotted. Then, the mean intensity and the interdistance of the peaks at 2 min and 15 min from the application of the stretching stimulus. The **Fig. 4.5 A** shows the cell cytoskeleton

under 8% and 29% strain levels. As suggested by the increment of actin intensity (**Fig. 4.5 B**), actin was recruited to reinforce SFs in response to substrate deformation. The enhanced contractility of cytoskeleton immediately after stretching was also supported by the remodeling of SFs whose interdistance decreased in the direction orthogonal to the stimulation (**Fig. 4.5 C**). The mean intensity of SFs was positively correlated with strain intensity, but a significant ($p < 0.01$, Appendix Tab. H) negative variation can be observed as a function of time in the case of the 29% strain.

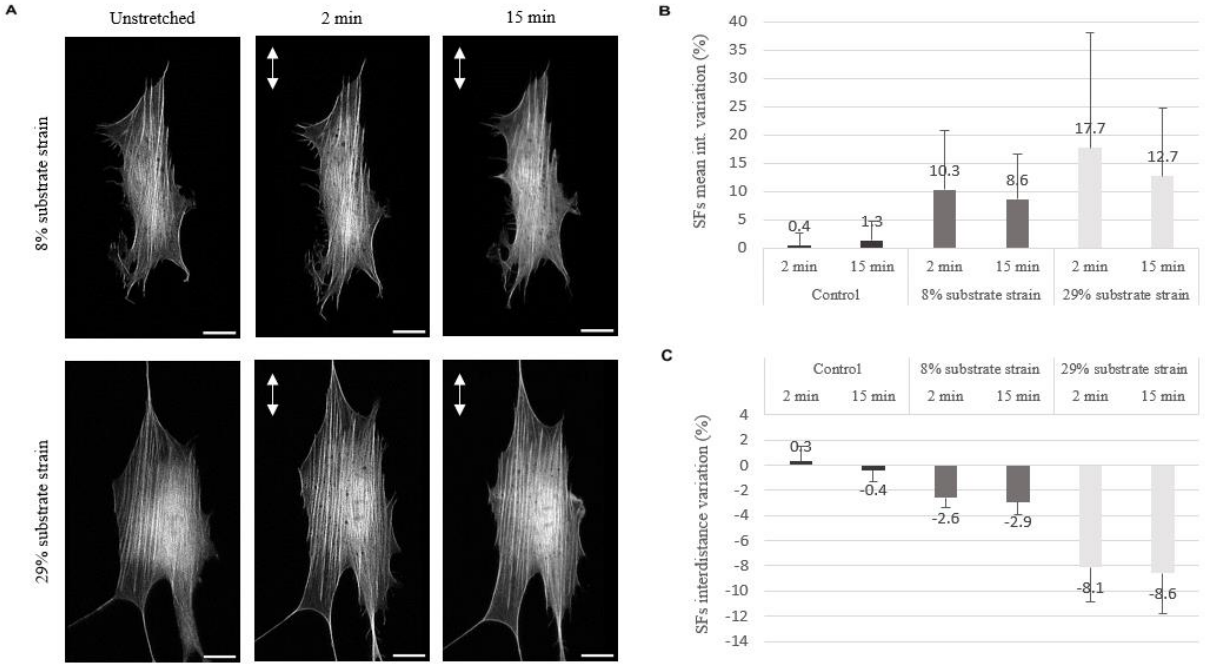

Fig. 4.5: *Cytoskeleton SFs response to sustained uniaxial substrate strain. A) Fluorescent images of NIH3T3 transfected with Lifeact subjected to 8% and 29% substrate strain levels. The white arrows indicate the stretching direction (scale bar = 20 µm). B) SFs mean intensity variations with respect to the initial condition as function of time and substrate strain. For statistical analysis see Appendix Tab. H. C) SFs interdistance variations in the direction orthogonal to the stretching direction as function of time and substrate strain. For statistical analysis see Appendix Tab. I. Error bars represent the standard error of the mean. N = 20 cells for the strain conditions (8% and 29% strain) and N = 6 cells for the control were analyzed over time.*

To evaluate the effects of the enhanced cytoskeleton tension on the nucleus, morphological parameters were extracted from nuclear images (**Fig. 4.6 A**). Cell stretching induced a significant increase (Appendix Tab. L) of nuclear longitudinal axes and a decrease of orthogonal axes as function of strain intensity (**Fig. 4.6 B**), resulting in more elongated nuclei (greater aspect ratio (AR)) in the strain direction (**Fig. 4.6 C**). These results reveal the main role of lateral compressive forces of the actin cytoskeleton in determining the nuclear deformation under the cell-substrate stretching condition. These deformations also prompted a significant (Appendix Tab. N) nuclear spreading area with respect to unstretched control nuclei (**Fig. 4.6 D**). However, in accordance with the FAs and cytoskeletal responses, nuclear area significantly ($p < 0.01$) decreased after 15 min under 29% strain while remained stable for 8% strain level, evidencing the strong interconnection between cell

mechanosensory components.

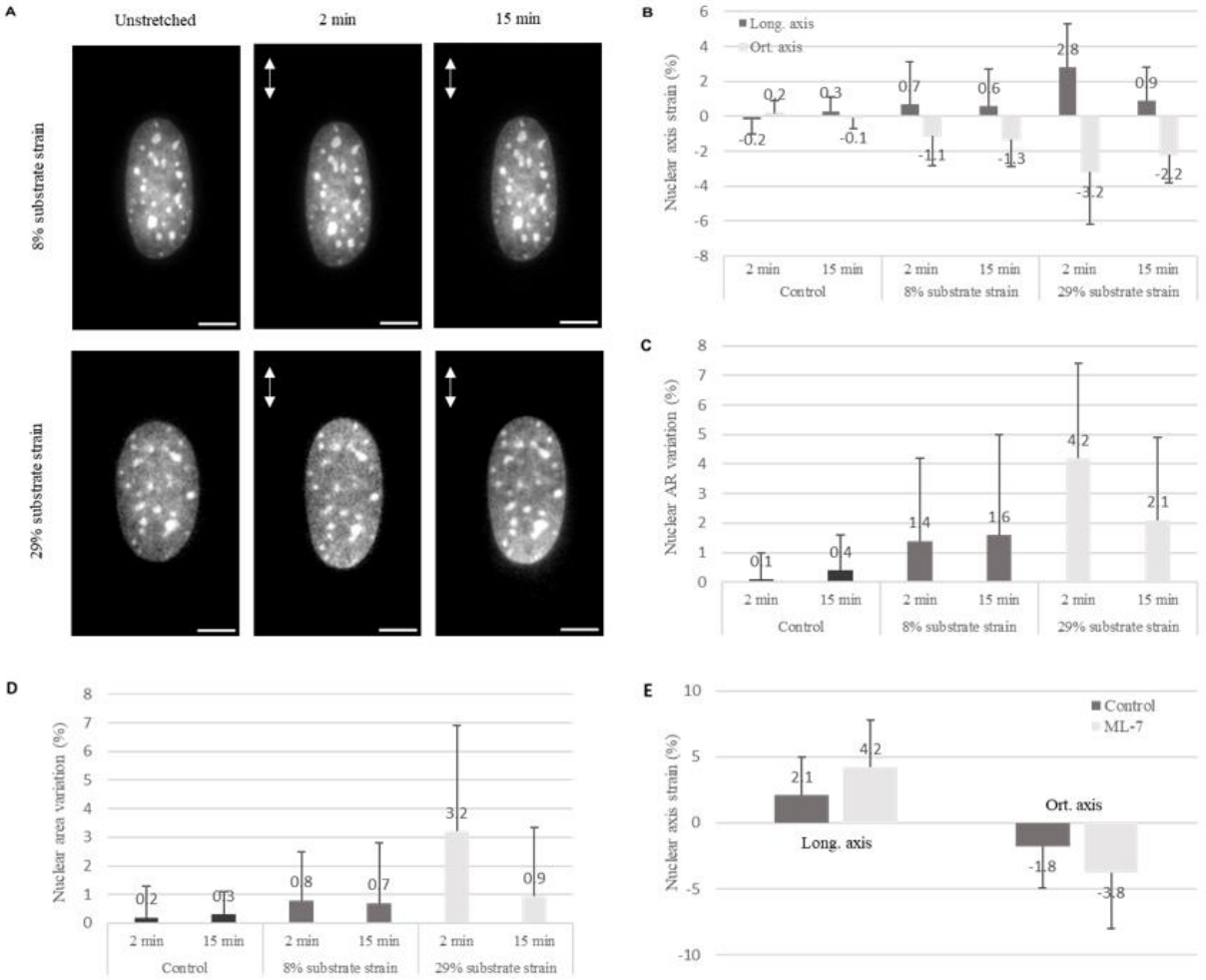

Fig. 4.6: *Morphological nuclear changes induced by sustained uniaxial substrate strain. A) Fluorescent images of cell nuclei subjected to 8% and 29% substrate strain levels. The white arrows indicate the stretching direction (scale bar = 10 µm). B) Nuclear longitudinal and orthogonal axis (respect the stretching direction) changes respect the initial configuration as function of time and substrate strain. For statistical analysis see Tab. L. C) Nuclear aspect ratio (AR) variations as function of time and substrate strain. For statistical analysis see Tab. M. D) Nuclear area variations as function of time and substrate strain. For statistical analysis see Tab. N. E) Nuclear longitudinal and orthogonal strains of cells treated with ML-7 and control cells subjected to 16% uniaxial substrate strain. For statistical analysis see Tab. O. The analysis was conducted at 2 min from the application of the stretching stimulus. Error bars represent the standard error of the mean. N = 20 nuclei for the strain conditions (8% and 29% strain) and N = 6 nuclei for the control were analyzed over time.*

The results shown in this work demonstrate that substrate strains are effectively transferred to the nucleus by means of the dynamic modulation of SFs forces, offering a quantitative characterization of this relationship. Contrary to FAs, nuclear deformations did not match those applied to the substrate as the mechanical stimuli are transferred to the nucleus not in a direct manner. In particular, even in response to high strain intensity, nuclear deformations were relatively low (< 3.2 %). One possible explanation could be related to the elevated nuclear prestress which characterizes cells on stiff substrates. This prestress is primarily generated by the cytoskeletal network which exert contractile

forces on the nuclear envelope, contributing to maintaining the structural integrity and shape of the nucleus under normal physiological conditions. Drescoll et al.[36] observed an inverse relationship between the prestress of the nucleus and its deformability in response to external stimuli. In agreement with these findings, we demonstrated that pharmacologically decreasing cytoskeleton contractility with ML7 resulted in an increase of nuclear deformation with applied stretch (**Fig. 4.6 E)**. In this context, we hypnotize that the same result could be achieve by decreasing the stiffness of the substrate on which the cells reside. A softer substrate imposes lower levels of cytoskeleton actomyosin contractility which could correlate with a more efficient control of the nuclear deformations through substrate stretching and the related mechanotransduction pathways.

4.6. Long-term cell response to substrate strain

To evaluate the cellular mechanical state following the complete mechanotransduction of the stretching signal, we measured the morphological parameters of cells and subcellular components after 2 h from the stimulation. The increase of cellular and nuclear spreading area passing from unstretched to stretched substrate has been already reported in the literature[10,37,38]. Here we found cells subjected to 8% sustained substrate stretching to have areas increments significantly ($p < 0.01$) higher than unstretched cells, while no significant difference was observed between 29% strain and control conditions (**Fig. 4.7 A**). As shown in **Fig. 4.7 B,** a similar significant ($p < 0.05$) trend was also obtained evaluating the spreading area variation of the nucleus, proving a not direct relationship with substrate strain intensity.

On the other hand, although larger cell spreading areas often correlate with larger FAs[39,40], the increase of cell area under 8% substrate stretching did not trigger a significant FAs length increment after 2h (**Fig. 4.8 E**). This could be explained considering that in our case cells are cultured on a stiff and nanopatterned substrate, both features that are known to induce large and elongated FAs[41,42]. In this way, FAs size could have reached a saturation point which can't be further perturbed through stretching. At the same time, both 8% and 29% strain levels did not affect cell and nuclear elongation (**Fig. 4.7 C, D**).

Although only partially, the long-term observations correlate with the cellular transient response shortly after the application of the stretching stimuli. The 8% strain was stably integrated by the cell mechanosensing apparatus and initiated mechanotransduction events that eventually led to reorganization of cytoskeleton and nuclear structure. Conversely, the high strain load triggered a

partial loss of the induced cellular deformation already after 15 min and induced a cell mechanical configuration similar to the one assumed on the unstretched substrate after 2 h. This adaptive response may be related to an unsustainable increment in tension generated within the cells and it may be aimed at maintaining cellular structural integrity and homeostasis.

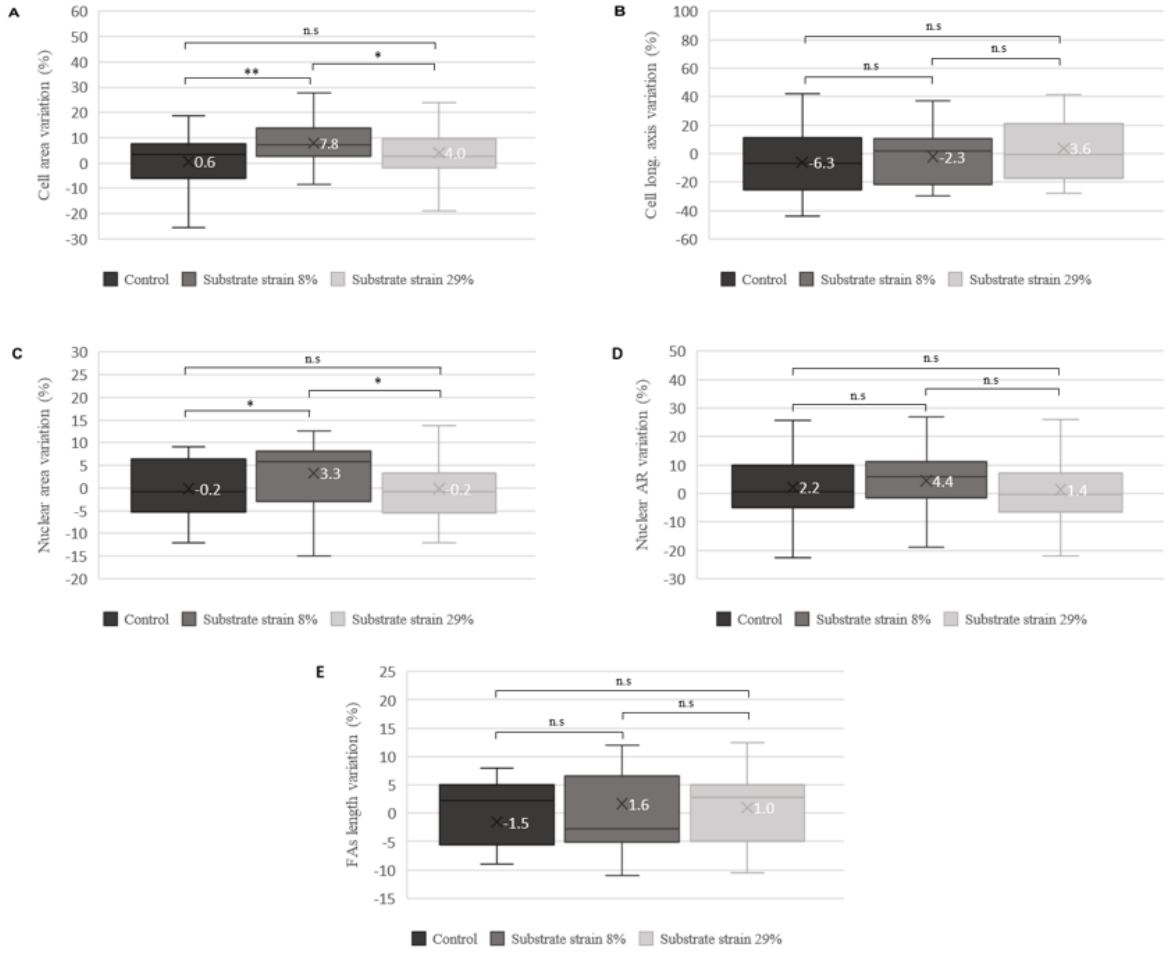

Fig. 4.7: *Morphological analysis of cells subjected to 2 h of sustained uniaxial strain . A) Cell spreading area changes as function of substrate strain. B) Cell longitudinal axis variations as function of substrate strain. C) Nuclear spreading area variations as function of substrate strain. D) Nuclear AR variations as function of substrate strain. E) FAs length variations as function of substrate strain. All the analyses were conducted at 2 h from the application of the stimulus. Error bars represent the standard error of the mean (cross). ** = p < 0.01, * = p < 0.05, n.s = not significant. N = 60 cells for each strain condition (0%, 8% and 29% strain) in two independent experiments for cell and nuclear morphological analyses. N = 10 cells for each condition for FAs morphological analysis.*

4.7. Discussion

Cell stretching represents a powerful and versatile technique to dynamically stimulate cells and to study the related cell mechanobiological response. By administering different spatial and temporal

stretching patterns to the cells seeded on an elastic substrate, cell stretching has been reported to affect multiple cellular functions[43,44]. However, in which entity the substrate strain is perceived by the cellular adhesion sites and propagated at cytoskeletal and nuclear level has not been fully characterized yet. To this aim, in this study we evaluated the dynamic response of cell mechanosensory apparatus to uniaxial strain.

Firstly, we characterized the correct transmission of substrate deformations to cells by analyzing the induced spatial displacement of FAs and the spreading area changes. A similar analysis was conducted by Sigaut et al.[45], who reported the spreading area of mammary epithelial living cells (HC11 cell line) measured from sequence of transmission microscopy cell images at increasing biaxial strain values. They showed that the average cell area follows, within errors, the substrate area increments. Our results partially deviate from these findings and evidence that substrates strains are efficiently transmitted to cells in terms of FAs spatial displacement, but the latter doesn't produce the expected cell area increments as the cell-material connection occurs only through discontinuous adhesion sites.

At the same time, we evaluated the FAs response to stretching also at a molecular level by monitoring the dynamic of different adhesion proteins. Given its presence in all the maturation stages of FAs, paxillin is a widely used molecule in literature to tag FAs with fluorescent molecules and evaluate their behavior for multiple applications[46,47]. However, in this work we demonstrated its inadequacy as an indicator of FAs growth and adhesion strength immediately after stretching Indeed, we showed that paxillin is mechanoresponsively recruited at strained SFs, preventing a reliable monitoring of FAs morphological and intensity changes following stretching. Conversely, by marking FAs with talin, we were able to confirm that substrate deformations are effectively transmitted to FAs in terms of length strains.

Forces perceived at FAs level were eventually propagated through the cytoskeleton SFs and converted to nuclear deformations. Although in this case we didn't obtain an alignment with substrate strain level, nuclear elongation was found to be in a direct relationship with the latter and supported by increments in SFs tension.

The observations over time attested the importance of the transient response, triggered shortly after the application of the mechanical stimulus, in dictating the following mechanotransduction events.

In particular, our results showed that the 8% strain level induced persistent changes in mechanosensory components over a period of 15 min that can explain the significant increase of cell and nuclear spreading area observed after 2h. These findings are supported by literature studies in which it is reported that cytoskeletal tension increments stimulate actin polymerization and cytoskeleton reinforcement[48] and that nuclear deformations can lead to changes in the chromatin

structure that affect nuclear shape and size[49].

At the same time, excessive loads on cells can induce mechanical instability and DNA damages, inducing cell protective mechanisms[50]. Conforming to this, we assume that cells under 29% stretching gradually dissipated the mechanical stimulus over the 2 h to restore a stable mechanical configuration.

In conclusion, these results highlight the existence of effective ranges and thresholds in mechanical stimulation to affect cellular mechanical configuration and, consequently, their mechanobiological response. In order to identify them, in this study we have provided a meticulous and quantitative approach to calibrate the mechanical stimuli delivered to cells that can be generalized for any cell type and mechanobiological applications.

4.8. References

1. Maurer, M. & Lammerding, J. The Driving Force: Nuclear Mechanotransduction in Cellular Function, Fate, and Disease. *Annu. Rev. Biomed. Eng.* **21**, 443–468 (2019).

2. Discher, D. E., Janmey, P. & Wang, Y. Tissue Cells Feel and Respond to the Stiffness of Their Substrate. *Science* **310**, 1139–1143 (2005).

3. Kuo, J.-C., Han, X., Hsiao, C.-T., Yates Iii, J. R. & Waterman, C. M. Analysis of the myosin-II-responsive focal adhesion proteome reveals a role for β-Pix in negative regulation of focal adhesion maturation. *Nat. Cell Biol.* **13**, 383–393 (2011).

4. Yoshigi, M., Hoffman, L. M., Jensen, C. C., Yost, H. J. & Beckerle, M. C. Mechanical force mobilizes zyxin from focal adhesions to actin filaments and regulates cytoskeletal reinforcement. *J. Cell Biol.* **171**, 209–215 (2005).

5. Yamashita, H. *et al.* Interaction of the vinculin proline-rich linker region with vinexin α in sensing extracellular matrix stiffness. *J. Cell Sci.* jcs.133645 (2014) doi:10.1242/jcs.133645.

6. Pasapera, A. M., Schneider, I. C., Rericha, E., Schlaepfer, D. D. & Waterman, C. M. Myosin II activity regulates vinculin recruitment to focal adhesions through FAK-mediated paxillin phosphorylation. *J. Cell Biol.* **188**, 877–890 (2010).

7. Carisey, A. *et al.* Vinculin Regulates the Recruitment and Release of Core Focal Adhesion Proteins in a Force-Dependent Manner. *Curr. Biol.* **23**, 271–281 (2013).

8. Neelam, S. *et al.* Direct force probe reveals the mechanics of nuclear homeostasis in the mammalian cell. *Proc. Natl. Acad. Sci.* **112**, 5720–5725 (2015).

9. Booth-Gauthier, E. A., Alcoser, T. A., Yang, G. & Dahl, K. N. Force-Induced Changes in Subnuclear Movement and Rheology. *Biophys. J.* **103**, 2423–2431 (2012).

10. Panzetta, V., Fusco, S. & Netti, P. A. Cell mechanosensing is regulated by substrate strain energy rather than stiffness. *Proc. Natl. Acad. Sci.* **116**, 22004–22013 (2019).

11. Wu, S. Y., Kim, W. & Kremen, T. J. In Vitro Cellular Strain Models of Tendon Biology and Tenogenic Differentiation. *Front. Bioeng. Biotechnol.* **10**, 826748 (2022).

12. Yu, H.-S., Kim, J.-J., Kim, H.-W., Lewis, M. P. & Wall, I. Impact of mechanical stretch on the cell behaviors of bone and surrounding tissues. *J. Tissue Eng.* **7**, 204173141561834 (2016).

13. Park, J.-A., Fredberg, J. J. & Drazen, J. M. Putting the Squeeze on Airway Epithelia. *Physiology* **30**, 293–303 (2015).

14. Li, Y. *et al.* An approach to quantifying 3D responses of cells to extreme strain. *Sci. Rep.* **6**, 19550 (2016).

15. Maiti, R. *et al.* In vivo measurement of skin surface strain and sub-surface layer deformation induced by natural tissue stretching. *J. Mech. Behav. Biomed. Mater.* **62**, 556–569 (2016).

16. Anwar, M. A., Shalhoub, J., Lim, C. S., Gohel, M. S. & Davies, A. H. The Effect of Pressure-Induced Mechanical Stretch on Vascular Wall Differential Gene Expression. *J. Vasc. Res.* **49**, 463–478 (2012).

17. Estrada, J. B., Cramer, H. C., Scimone, M. T., Buyukozturk, S. & Franck, C. *Neural cell injury pathology due to high-rate mechanical loading.* http://biorxiv.org/lookup/doi/10.1101/2021.05.12.443823 (2021) doi:10.1101/2021.05.12.443823.

18. Oakes, P. W. & Gardel, M. L. Stressing the limits of focal adhesion mechanosensitivity. *Curr. Opin. Cell Biol.* **30**, 68–73 (2014).

19. Stehbens, S. J. & Wittmann, T. Analysis of focal adhesion turnover. in *Methods in Cell Biology* vol. 123 335–346 (Elsevier, 2014).

20. Boccafoschi, F., Bosetti, M., Gatti, S. & Cannas, M. Dynamic Fibroblast Cultures: Response to Mechanical Stretching. *Cell Adhes. Migr.* **1**, 124–128 (2007).

21. Chen, Y., Pasapera, A. M., Koretsky, A. P. & Waterman, C. M. Orientation-specific responses to sustained uniaxial stretching in focal adhesion growth and turnover. *Proc. Natl. Acad. Sci.* **110**, (2013).

22. Tsukamoto, S. *et al.* Compressive forces driven by lateral actin fibers are a key to the nuclear deformation under uniaxial cell-substrate stretching. *Biochem. Biophys. Res. Commun.* **597**, 37–43 (2022).

23. Ives, C. L., Eskin, S. G. & McIntire, L. V. Mechanical effects on endothelial cell morphology: In vitro assessment. *In Vitro Cell. Dev. Biol.* **22**, 500–507 (1986).

24. De, R., Zemel, A. & Safran, S. A. Dynamics of cell orientation. *Nat. Phys.* **3**, 655–659 (2007).

25. Nekouzadeh, A., Pryse, K. M., Elson, E. L. & Genin, G. M. Stretch-activated force shedding, force recovery, and cytoskeletal remodeling in contractile fibroblasts. *J. Biomech.* **41**, 2964–2971 (2008).

26. Hinkle, E. R. *et al.* Stretching muscle cells induces transcriptional and splicing transitions and changes in SR proteins. *Commun. Biol.* **5**, 987 (2022).

27. Xie, W. *et al.* Static and Dynamic: Evolving Biomaterial Mechanical Properties to Control

Cellular Mechanotransduction. *Adv. Sci.* **10**, 2204594 (2023).

28. Swaminathan, V. & Waterman, C. M. The molecular clutch model for mechanotransduction evolves. *Nat. Cell Biol.* **18**, 459–461 (2016).

29. Schiller, H. B., Friedel, C. C., Boulegue, C. & Fässler, R. Quantitative proteomics of the integrin adhesome show a myosin II-dependent recruitment of LIM domain proteins. *EMBO Rep.* **12**, 259–266 (2011).

30. Turner, C. E. Paxillin interactions. *J. Cell Sci.* **113**, 4139–4140 (2000).

31. Sawada, Y. & Sheetz, M. P. Force transduction by Triton cytoskeletons. *J. Cell Biol.* **156**, 609–615 (2002).

32. Smith, M. A. *et al.* LIM Domains Target Actin Regulators Paxillin and Zyxin to Sites of Stress Fiber Strain. *PLoS ONE* **8**, e69378 (2013).

33. Tajik, A. *et al.* Transcription upregulation via force-induced direct stretching of chromatin. *Nat. Mater.* **15**, 1287–1296 (2016).

34. Uhler, C. & Shivashankar, G. V. Regulation of genome organization and gene expression by nuclear mechanotransduction. *Nat. Rev. Mol. Cell Biol.* **18**, 717–727 (2017).

35. Ingber, D. E. The riddle of morphogenesis: A question of solution chemistry or molecular cell engineering? *Cell* **75**, 1249–1252 (1993).

36. Driscoll, T. P., Cosgrove, B. D., Heo, S.-J., Shurden, Z. E. & Mauck, R. L. Cytoskeletal to Nuclear Strain Transfer Regulates YAP Signaling in Mesenchymal Stem Cells. *Biophys. J.* **108**, 2783–2793 (2015).

37. Chowdhury, F. *et al.* Material properties of the cell dictate stress-induced spreading and differentiation in embryonic stem cells. *Nat. Mater.* **9**, 82–88 (2010).

38. Aragona, M. *et al.* A Mechanical Checkpoint Controls Multicellular Growth through YAP/TAZ Regulation by Actin-Processing Factors. *Cell* **154**, 1047–1059 (2013).

39. Saez, A., Buguin, A., Silberzan, P. & Ladoux, B. Is the Mechanical Activity of Epithelial Cells Controlled by Deformations or Forces? *Biophys. J.* **89**, L52–L54 (2005).

40. Ghibaudo, M. *et al.* Traction forces and rigidity sensing regulate cell functions. *Soft Matter* **4**, 1836 (2008).

41. Yeung, T. *et al.* Effects of substrate stiffness on cell morphology, cytoskeletal structure, and adhesion. *Cell Motil. Cytoskeleton* **60**, 24–34 (2005).

42. Natale, C. F., Ventre, M. & Netti, P. A. Tuning the material-cytoskeleton crosstalk via

nanoconfinement of focal adhesions. *Biomaterials* **35**, 2743–2751 (2014).

43. Constantinou, I. & Bastounis, E. E. Cell-stretching devices: advances and challenges in biomedical research and live-cell imaging. *Trends Biotechnol.* **41**, 939–950 (2023).

44. Zhao, J., Meng, F., Qian, J., Huang, Y. & Fan, Y. In vitro cell stretching devices and their applications: From cardiomyogenic differentiation to tissue engineering. *Med. Nov. Technol. Devices* **18**, 100220 (2023).

45. Sigaut, L. *et al.* Live cell imaging reveals focal adhesions mechanoresponses in mammary epithelial cells under sustained equibiaxial stress. *Sci. Rep.* **8**, 9788 (2018).

46. Hu, Y.-L. *et al.* FAK and paxillin dynamics at focal adhesions in the protrusions of migrating cells. *Sci. Rep.* **4**, 6024 (2014).

47. Donato, D. M., Ryzhova, L. M., Meenderink, L. M., Kaverina, I. & Hanks, S. K. Dynamics and Mechanism of p130Cas Localization to Focal Adhesions. *J. Biol. Chem.* **285**, 20769–20779 (2010).

48. Burridge, K. & Guilluy, C. Focal adhesions, stress fibers and mechanical tension. *Exp. Cell Res.* **343**, 14–20 (2016).

49. Kalukula, Y., Stephens, A. D., Lammerding, J. & Gabriele, S. Mechanics and functional consequences of nuclear deformations. *Nat. Rev. Mol. Cell Biol.* **23**, 583–602 (2022).

50. Seelbinder, B. *et al.* TENSCell: Imaging of Stretch-Activated Cells Reveals Divergent Nuclear Behavior and Tension. *Biophys. J.* **118**, 2627–2640 (2020).

Chapter 5

Final conclusions and future prospectives

In the field of mechanobiology, the efforts are concentrated in understanding how to effectively manipulate mechanical cues in order to dictate cell functions and fate. Over the past few decades, multiple *in vitro* cell stimulation devices have been developed in an effort to better understand the complex interplay between mechanical stimuli and cellular responses. Although these tools have demonstrated the substantial impact of mechanical signals such as shear stress, matrix rigidity, compression, and tension on diverse cellular functions[1–4], the direct correlation between the external forces actually sensed by cells and their corresponding biological response remains elusive. Indeed, the mechanical heterogeneity that characterizes cells in the standard culture systems hinders the identification of univocal cellular responses to the externally applied stimuli.

To overcome these challenges, in this PhD thesis we developed an innovative tool able to standardize cell perception of mechanical stimulation. More specifically, an electromechanical actuation system was realized to deliver highly controlled deformations to a PDMS cell stretching chamber. A control over cell orientation was then implemented through the integration of nanogrooves on the elastic membrane on which cells are seeded. In this way all the subcellular mechanosensory components were polarized along the direction of the solicitation, standardizing the stretching stimuli administered to the cells.

The device integration with microscope stage and incubator was fundamental for monitoring the real-time cell response in live cell experiments. We demonstrated that, immediately after stretching, substrate deformations are efficiently perceived at FAs level and converted into nuclear deformations through the consequent increment of cytoskeletal contractility. A strain level dependent cell response was then observed as a function of time. Increments of intracellular tension, induced by the stretching of the substrate, within the cell physiological limits positively correlated with increments of cell and nuclear spreading areas. Conversely, the excessive strain load was not able to induce long-term changes in the cell mechanical configuration.

In conclusion, in this work, we presented a novel and versatile tool which can enhance the comprehension of the complex relationship between mechanical signals and cell biological responses. By applying controlled and univocal mechanical doses to the cells, it could be exploited to identify

the effective ranges of stimulation to affect various cellular functions such as migration, proliferation and differentiation. For this purpose, in the subsequent studies we could focus on assessing the molecular mechanisms that regulate the transduction of external signals in terms of transcription factor flux and the expression of specific genes. Moreover, it would be interesting to evaluate the effects on cell response of multiple stimulation variables in addition to strain magnitude. Stretching in the direction orthogonal to the cell polarization one on the nanopatterned substrate, for example, could lead to results completely different from the ones achieved in this work. Indeed, in these conditions, substrate strains would be transferred to the cell nuclei minimizing the elongation of the FAs and stress fibers. Furthermore, the velocity of substrate stretching could significantly impact on the temporal dynamics of cellular mechanoresponse. Slower stretching velocities may provide more time for the cells to gradually and dynamically adapt, in terms of FAs remodeling and cytoskeletal rearrangement, to high substrate strains. According to that, Horvath et al.[1] demonstrated also that slow rate stretching induce nuclear area increments significantly higher and more stable in time than the one of cells stretched at a higher rate.

Regarding the cell stretching system, an important advancement would be its automatization. By harnessing the capabilities of automation for image acquisition of cell response and data analysis, it could be possible to conduct high-throughput studies and improve experimental reproducibility and reliability. A further step forward would be the integration of a feedback control system in the stretching device to dynamically adjust stretching parameters in real-time based on cellular responses. This adaptive control could enable the optimization of stretching conditions to achieve desired outcomes, such as inducing specific cellular behaviors and dictating cell fate.

The knowledge coming from these studies would be pivotal for developing innovative mechano-therapeutic strategies and improving outcomes in areas such as tissue engineering and mechanomedicine.

5.1. References

1. Liu, J. *et al.* Shear stress regulates endothelial cell autophagy via redox regulation and Sirt1 expression. *Cell Death Dis.* **6**, e1827–e1827 (2015).

2. Tiskratok, W. *et al.* Substrate stiffness controls proinflammatory responses in human gingival fibroblasts. *Sci. Rep.* **13**, 1358 (2023).

3. Onal, S., Alkaisi, M. M. & Nock, V. Microdevice-based mechanical compression on living cells. *iScience* **25**, 105518 (2022).

4. Gossett, D. R. *et al.* Hydrodynamic stretching of single cells for large population mechanical phenotyping. *Proc. Natl. Acad. Sci.* **109**, 7630–7635 (2012).

5. Horvath, A. N. *et al.* Focus on time: dynamic imaging reveals stretch-dependent cell relaxation and nuclear deformation. *Biophys. J.* **120**, 764–772 (2021).

Appendix

Statistical analysis

Data are reported as mean ± SEM. Statistical comparisons were performed with a Student's unpaired test. *P* values of <0.05 denote statistically significant difference.

Fig. 4.2

Tab. A

			Talin						**Paxillin**					
			Control		Substrate strain 8%		Substrate strain 29%		Control		Substrate strain 8%		Substrate strain 29%	
			2 min	15 min	2 min	15 min	2 min	15 min	2 min	15 min	2 min	15 min	2 min	15 min
Talin	Control	2 min		n.s	**	**	**	**	n.s	n.s	**	**	**	**
		15 min			**	**	**	**		n.s	**	**	**	**
	Substrate strain 8%	2 min				n.s	**	**			n.s	n.s	**	**
		15 min					**	**				n.s	**	**
	Substrate strain 29%	2 min						*					n.s	*
		15 min												n.s
Paxillin	Control	2 min								n.s	**	**	**	**
		15 min									**	**	**	**
	Substrate strain 8%	2 min										n.s	**	**
		15 min											**	**
	Substrate strain 29%	2 min												*
		15 min												

Tab. B

		Control		Substrate strain 8%		Substrate strain 29%	
		2 min	15 min	2 min	15 min	2 min	15 min
Control	2 min		n.s	**	**	**	**
	15 min			**	**	**	**
Substrate strain 8%	2 min				n.s	**	**
	15 min					**	**
Substrate strain 29%	2 min						*
	15 min						

Fig. 4.3

Tab. C

			Talin						**Paxillin**					
			Control		Substrate strain 8%		Substrate strain 29%		Control		Substrate strain 8%		Substrate strain 29%	
			2 min	15 min	2 min	15 min	2 min	15 min	2 min	15 min	2 min	15 min	2 min	15 min
Talin	Control	2 min		n.s	**	**	**	**	n.s	n.s	**	**	**	**
		15 min			**	**	**	**		n.s	**	**	**	**
	Substrate strain 8%	2 min				n.s	**	**			**	n.s	**	**
		15 min					**	**				n.s	**	**
	Substrate strain 29%	2 min						*					**	n.s
		15 min												n.s
Paxillin	Control	2 min								n.s	**	**	**	**
		15 min									**	**	**	**
	Substrate strain 8%	2 min										**	**	**
		15 min											**	**
	Substrate strain 29%	2 min												**
		15 min												

Tab. D

			Talin						**Paxillin**					
			Control		Substrate strain 8%		Substrate strain 29%		Control		Substrate strain 8%		Substrate strain 29%	
			2 min	15 min	2 min	15 min	2 min	15 min	2 min	15 min	2 min	15 min	2 min	15 min
Talin	Control	2 min		n.s	**	**	**	**	n.s	n.s	**	**	**	**
		15 min			**	**	**	**		n.s	**	**	**	**
	Substrate strain 8%	2 min				n.s	**	**			**	**	**	**
		15 min					**	**				**	**	**
	Substrate strain 29%	2 min						n.s					**	**
		15 min												**
Paxillin	Control	2 min								n.s	**	**	**	**
		15 min									**	**	**	**
	Substrate strain 8%	2 min										**	**	n.s
		15 min											**	**
	Substrate strain 29%	2 min												**
		15 min												

Fig. 4.4

Tab. E

			"Coherent" FAs						"Incoherent" FAs					
			Control		Substrate strain 8%		Substrate strain 29%		Control		Substrate strain 8%		Substrate strain 29%	
			2 min	15 min	2 min	15 min	2 min	15 min	2 min	15 min	2 min	15 min	2 min	15 min
"Coherent" FAs	Control	2 min		n.s	**	**	**	**			**	**	**	**
		15 min			**	**	**	**			**	**	**	**
	Substrate strain 8%	2 min				n.s	**	**			**	n.s	**	**
		15 min					**	**				n.s	**	**
	Substrate strain 29%	2 min						*					**	n.s
		15 min												*
"Incoherent" FAs	Control	2 min									**	**	**	**
		15 min									**	**	**	**
	Substrate strain 8%	2 min										**	**	**
		15 min											**	**
	Substrate strain 29%	2 min												**
		15 min												

Tab. F

			“Coherent” FAs						**“Incoherent” FAs**					
			Control		Substrate strain 8%		Substrate strain 29%		Control		Substrate strain 8%		Substrate strain 29%	
			2 min	15 min	2 min	15 min	2 min	15 min	2 min	15 min	2 min	15 min	2 min	15 min
“Coherent” FAs	Control	2 min		n.s	**	**	**	**			**	**	**	**
		15 min			**	**	**	**			**	**	**	**
	Substrate strain 8%	2 min				**	**	n.s			*	**	**	n.s
		15 min					**	**				n.s	**	**
	Substrate strain 29%	2 min						**					*	**
		15 min												n.s
“Incoherent” FAs	Control	2 min									**	**	**	**
		15 min									**	**	**	**
	Substrate strain 8%	2 min										**	**	n.s
		15 min											**	**
	Substrate strain 29%	2 min												**
		15 min												

Tab. G

			Talin-FAs					
			Control		Substrate strain 8%		Substrate strain 29%	
			2 min	15 min	2 min	15 min	2 min	15 min
"Coherent" Paxillin-FAs	Control	2 min	n.s	n.s	**	**	**	**
		15 min		n.s	**	**	**	**
	Substrate strain 8%	2 min			n.s	n.s	**	**
		15 min				n.s	**	**
	Substrate strain 29%	2 min					n.s	*
		15 min						n.s

Fig. 4.5

Tab. H

		Control		Substrate strain 8%		Substrate strain 29%	
		2 min	15 min	2 min	15 min	2 min	15 min
Control	2 min		n.s	**	**	**	**
	15 min			**	**	**	**
Substrate strain 8%	2 min				n.s	**	n.s
	15 min					**	*
Substrate strain 29%	2 min						**
	15 min						

Tab. I

		Control		Substrate strain 8%		Substrate strain 29%	
		2 min	15 min	2 min	15 min	2 min	15 min
Control	2 min		n.s	**	**	**	**
	15 min			**	**	**	**
Substrate strain 8%	2 min				n.s	**	**
	15 min					**	**
Substrate strain 29%	2 min						n.s
	15 min						

Fig. 4.6

Tab. L

			Long. axis						Ort. axis					
			Control		Substrate strain 8%		Substrate strain 29%		Control		Substrate strain 8%		Substrate strain 29%	
			2 min	15 min	2 min	15 min	2 min	15 min	2 min	15 min	2 min	15 min	2 min	15 min
Long. axis	Control	2 min		n.s	**	**	**	**	n.s	n.s	**	**	**	**
		15 min			**	**	**	**		n.s	**	**	**	**
	Substrate strain 8%	2 min				n.s	**	n.s			**	**	**	**
		15 min					**	n.s				**	**	**
	Substrate strain 29%	2 min						**					**	**
		15 min												**
Ort. axis	Control	2 min									**	**	**	**
		15 min									**	**	**	**
	Substrate strain 8%	2 min										n.s	**	n.s
		15 min											**	n.s
	Substrate strain 29%	2 min												*
		15 min												

Tab. M

		Control		Substrate strain 8%		Substrate strain 29%	
		2 min	15 min	2 min	15 min	2 min	15 min
Control	2 min		n.s	**	**	**	**
	15 min			**	**	**	**
Substrate strain 8%	2 min				n.s	**	n.s
	15 min					**	n.s
Substrate strain 29%	2 min						**
	15 min						

Tab. N

		Control		Substrate strain 8%		Substrate strain 29%	
		2 min	15 min	2 min	15 min	2 min	15 min
Control	2 min		n.s	**	**	**	**
	15 min			**	**	**	**
Substrate strain 8%	2 min				n.s	**	n.s
	15 min					**	n.s
Substrate strain 29%	2 min						**
	15 min						

Tab. O

		Control		ML-7	
		Long. axis	Ort. axis	Long. axis	Ort. axis
Control	Long. axis		**	*	**
	Ort. axis				*
ML-7	Long. axis				**
	Ort. axis				